

COCKPIT: A Practical Debugging Tool for Training Deep Neural Networks

Frank Schneider*
 University of Tübingen
 Maria-von-Linden-Straße 6
 Tübingen, Germany
 fschneider@tue.mpg.de

Felix Dangel*
 University of Tübingen
 Maria-von-Linden-Straße 6
 Tübingen, Germany
 fdangel@tue.mpg.de

Philipp Hennig
 University of Tübingen &
 MPI for Intelligent Systems
 Tübingen, Germany
 ph@tue.mpg.de

Abstract

When engineers train deep learning models, they are very much “flying blind”. Commonly used approaches for real-time training diagnostics, such as monitoring the train/test loss, are limited. Assessing a network’s training process solely through these performance indicators is akin to debugging software without access to internal states through a debugger. To address this, we present COCKPIT, a collection of instruments that enable a closer look into the inner workings of a learning machine, and a more informative and meaningful status report for practitioners. It facilitates the identification of learning phases and failure modes, like ill-chosen hyperparameters. These instruments leverage novel higher-order information about the gradient distribution and curvature, which has only recently become efficiently accessible. We believe that such a debugging tool, which we open-source for PYTORCH, represents an important step to improve troubleshooting the training process, reveal new insights, and help develop novel methods and heuristics.

1. Introduction & motivation

Deep learning represents a new programming paradigm: instead of deterministic programs, users design models and “simply” train them with data. In this metaphor, deep learning is a meta-programming form, where *coding* is replaced by *training*. Here, we ponder the question what a (better) debugger for this process should look like.

Debuggers are indispensable for traditional software development. When things fail unexpectedly, they give access to the internal workings of the code, allowing a look “into the box”. This is much more efficient than re-running the program with different inputs. And yet, the state-of-the-art in deep learning is arguably closer to the latter. If the attempt to train a deep net on a new data set fails, a machine learn-

ing engineer faces various options: Should they change the training hyperparameters (how?); the optimizer (to which one?); the architecture (how?); or just re-run with a different seed? Machine learning toolboxes provide scant help to guide these decisions.

Of course, traditional debuggers can be applied to deep learning. They will give access to every single weight of a neural network, or the individual pixels of its training data. But this rarely yields insights towards successful training. Extracting meaningful information requires a statistical approach and distillation of the bewildering complexity into a manageable summary. Tools like TENSORBOARD [1] were built in part to streamline this visualization. Yet, the quantities that are widely monitored (mainly train/test loss & accuracy), hardly provide useful feedback beyond a relative comparison among multiple training runs. They do not show the network’s internal state. Figure 1 illustrates how such established learning curves can describe the *current* state of the model – whether it is performing well or not – while failing to inform about training state and dynamics. They tell the user *that* things are going well or badly, but not *why*.

The situation is similar to flying a plane by observing only its altimeter. It is not surprising, then, that achieving state-of-the-art performance in deep learning requires expert intuition, or plain trial and error.

Here, we try to enrich the deep learning pipeline with a visual and statistical debugging tool. To this end, we propose new observables, in addition to using several established ones (Section 2). We leverage and augment recent extensions to automatic differentiation (in particular BACKPACK [11] for PYTORCH [29]) to efficiently access second-order statistical (e.g. gradient variances) and geometric (e.g. Hessian) information. We show how the proposed quantities can aid the deep learning software engineer in online tasks, like learning rate selection, as well as detecting common problems with data processing or model architectures (Section 3).

Concretely, we introduce COCKPIT, a flexible and efficient framework for monitoring these observables online dur-

*Equal contribution

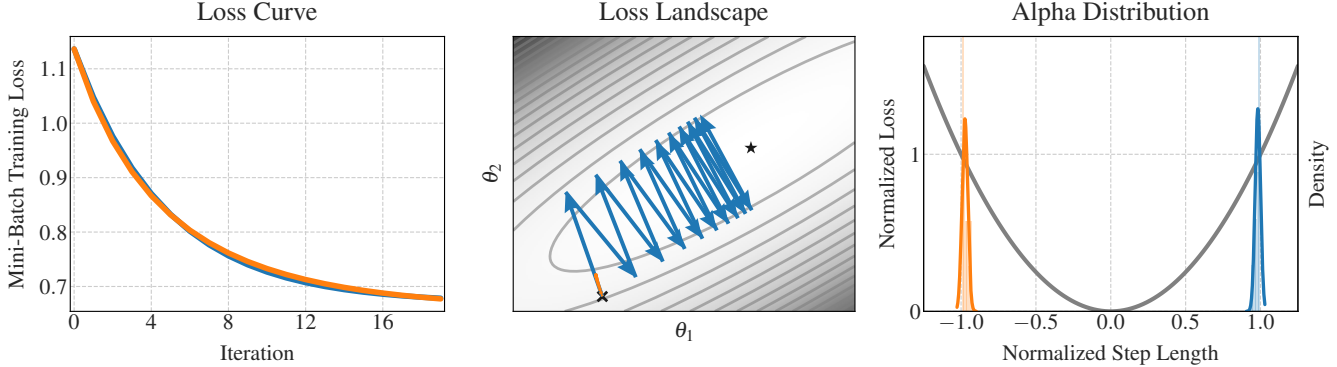


Figure 1. **Illustrative example: Learning curves do not tell the whole story.** Two different optimization runs (—/—) can lead to virtually the same loss curve (left). However, the actual optimization trajectories (middle), exhibit vastly different behaviors. In practice, they are intractably large and cannot be visualized directly. Recommendable actions for both scenarios (increase/decrease the learning rate) cannot be inferred from the loss curve. The α -distribution, one COCKPIT instrument (right), not only clearly distinguishes the two scenarios, but also allows for taking decisions regarding how the learning rate should be adapted. See Section 3.3 for further details.

ing training in carefully designed plots we call ‘‘instruments’’ (see Figure 2). To be of practical use, such visualization must have manageable computational overhead. We provide three different configurations of varying computational complexity and demonstrate that their instruments keep the computational cost *well below* a factor of 2 in run time (Section 4). COCKPIT scales well to real-world deep learning problems (see Figure 2 and Section 5). It is available at

<https://github.com/f-dangel/cockpit>,

open-source, extendable, and seamlessly integrates into conventional PYTORCH training loops.

2. COCKPIT’s instruments

Setting: We consider supervised regression/classification with labeled data $(\mathbf{x}, \mathbf{y}) \in \mathbb{X} \times \mathbb{Y}$ generated by a distribution $P(\mathbf{x}, \mathbf{y})$. The training set $\mathcal{D} = \{(\mathbf{x}_n, \mathbf{y}_n) \mid n = 1, \dots, N\}$ consists of N i.i.d. samples from P and the deep model $f : \Theta \times \mathbb{X} \rightarrow \mathbb{Y}$ maps inputs \mathbf{x}_n to predictions $\hat{\mathbf{y}}_n$ by parameters $\boldsymbol{\theta} \in \mathbb{R}^D$. This prediction is evaluated by a loss function $\ell : \mathbb{Y} \times \mathbb{Y} \rightarrow \mathbb{R}$ which compares to the label \mathbf{y}_n . The goal is minimizing an inaccessible expected risk $\mathcal{L}_P(\boldsymbol{\theta}) = \int \ell(f(\boldsymbol{\theta}, \mathbf{x}), \mathbf{y}) dP(\mathbf{x}, \mathbf{y})$ by empirical approximation through $\mathcal{L}_{\mathcal{D}}(\boldsymbol{\theta}) = \frac{1}{N} \sum_{n=1}^N \ell(f(\boldsymbol{\theta}, \mathbf{x}_n), \mathbf{y}_n) := \frac{1}{N} \sum_{n=1}^N \ell_n(\boldsymbol{\theta})$, which in practice though can only be stochastically subsampled on mini-batches $\mathcal{B} \subseteq \{1, \dots, N\}$,

$$\mathcal{L}_{\mathcal{B}}(\boldsymbol{\theta}) = \frac{1}{|\mathcal{B}|} \sum_{n \in \mathcal{B}} \ell_n(\boldsymbol{\theta}). \quad (1)$$

As is standard practice, we use first- and second-order information of the mini-batch loss, described by the mini-batch gradient as an average over individual gradients $\mathbf{g}_n(\boldsymbol{\theta})$,

$$\mathbf{g}_{\mathcal{B}}(\boldsymbol{\theta}) = \frac{1}{|\mathcal{B}|} \sum_{n \in \mathcal{B}} \underbrace{\nabla_{\boldsymbol{\theta}} \ell_n(\boldsymbol{\theta})}_{\mathbf{g}_n(\boldsymbol{\theta})}, \quad (2)$$

and the mini-batch Hessian

$$\mathbf{H}_{\mathcal{B}}(\boldsymbol{\theta}) = \frac{1}{|\mathcal{B}|} \sum_{n \in \mathcal{B}} \nabla_{\boldsymbol{\theta}}^2 \ell_n(\boldsymbol{\theta}). \quad (3)$$

Design choices: To minimize computational and design overhead, we restrict the metrics to quantities that require no additional model evaluations. This means that, at training step $t \rightarrow t + 1$ with mini-batches $\mathcal{B}_t, \mathcal{B}_{t+1}$ and parameters $\boldsymbol{\theta}_t, \boldsymbol{\theta}_{t+1}$, we may access information about the mini-batch losses $\mathcal{L}_{\mathcal{B}_t}(\boldsymbol{\theta}_t)$ and $\mathcal{L}_{\mathcal{B}_{t+1}}(\boldsymbol{\theta}_{t+1})$, but no cross-terms that would require additional forward passes.

Key point: $\mathcal{L}_{\mathcal{B}}(\boldsymbol{\theta}), \mathbf{g}_{\mathcal{B}}(\boldsymbol{\theta})$, and $\mathbf{H}_{\mathcal{B}}(\boldsymbol{\theta})$ are just expected values of a *distribution* over the batch. Only recently, this distribution has begun to attract attention [13] as its computation has become more accessible [7, 11]. Contemporary optimizers leverage only the *mean* gradient and neglect higher moments. One core point of our work is making extensive use of these distribution properties, trying to visualize them in various ways. This distinguishes COCKPIT from being ‘‘just a collection of plots’’ that could be built in tools like TENSORBOARD. Leveraging these distributional quantities, we create instruments and show how they can help adapt hyperparameters (Section 2.1), analyze the loss landscape (Section 2.2), and track network dynamics (Section 2.3). Instruments can sometimes be built from already-computed information or are efficient variants of previously proposed observables. To keep the presentation concise, we highlight the instruments shown in Figure 2 and listed in Table 1. Appendix B defines them formally and contains more extensions, such as the mean GSNR [24], the early stopping [25] and CABS [4] criterion, which can be used in COCKPIT.

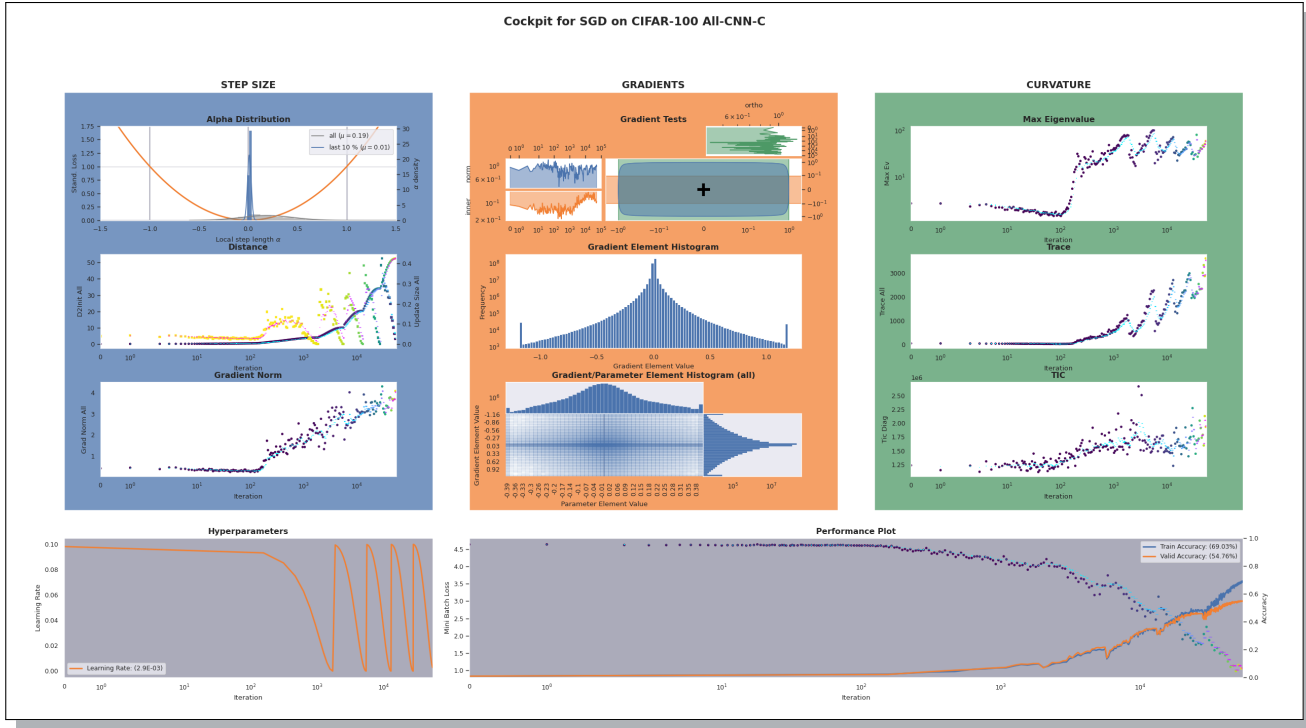


Figure 2. **Screenshot of COCKPIT’s full view** while training the ALL-CNN-C [36] on CIFAR-100 with SGD using a cyclical learning rate schedule. Figure and labels are not meant to be legible, but serve to give an impression of how COCKPIT looks to the user. Gray panels (bottom row) show the information currently tracked by most practitioners. The individual instruments are discussed in Section 2, and observations are described in Section 5. An animated version can be found in the accompanying GitHub repository.

2.1. Adapting hyperparameters

One of the biggest challenges in deep learning is setting the hyperparameters correctly. Currently, this choice is mostly done by trial and error through parameter searches. We aim to augment this process by providing a set of instruments to inform the user about what effect the selected hyperparameters have on the current training process.

Alpha: Are we crossing the valley? Using individual loss and gradient information at the start and end point of each iteration, we build a noise-informed univariate quadratic approximation along the step direction (*i.e.* the loss as a function of the step-size), and assess to which point on this parabola our optimizer moves. We standardize this value α such that stepping to the valley-floor is assigned $\alpha = 0$, the starting point is at $\alpha = -1$ and updates to the point exactly opposite of the starting point have $\alpha = 1$ (compare right panel of Figure 1). In Section 3.3 we demonstrate empirically that, counter-intuitively, it is generally *not* a good idea to choose the learning rate such that $\alpha \approx 0$.

Figure 1 illustrates the scenarios $\alpha = \pm 1$ and how monitoring the α -distributions can help distinguish between two training runs with similar performance but distinct failure sources. By default, this COCKPIT instrument shows the

α -distribution for both the last 10 % of training as well as the full training process (*e.g.* top left plot in Figure 2).

Distances: Are we making progress? Another way to discern the trajectories in Figure 1 is by measuring the *distance to initialization* in parameter space [28], and *update size* [2, 14]. Both are shown together in one COCKPIT instrument (*e.g.* center left plot in Figure 2) and would be significantly larger for the blue trajectory.

These distances are also able to disentangle phases in the blue trajectory. Using the same learning rate, it will continue to “jump back and forth” between the loss valley’s walls but at some point cease to make progress towards the minimum. During the initial phase of “surfing the wall”, *distance from initialization* increases. Ultimately though, it will stagnate, while the *update size* remains non-zero, indicating diffusion. While the initial “surfing the wall”-phase benefits successful training (see Section 3.3), achieving stationarity may require adaptation once the optimizer reaches that diffusion.

Gradient norm: How steep is the wall? The *update size* will show that the orange trajectory is stuck. But why? Such slow-down can result from both a bad learning rate and from loss landscape plateaus. The *gradient norm* (bottom left

Name	Description	Min. Config
Alpha	Normalized step on a noisy quadratic interpolation between two iterates θ_t, θ_{t+1}	<i>economy</i>
Distance	Update size $\ \theta_{t+1} - \theta_t\ $ and distance from initialization $\ \theta_t - \theta_0\ $	<i>economy</i>
GradNorm	Mini-batch gradient norm $\ \mathbf{g}_{\mathcal{B}}(\theta)\ $	<i>economy</i>
NormTest	Normalized fluctuations of the residual norms $\ \mathbf{g}_{\mathcal{B}} - \mathbf{g}_n\ $, proposed in [8]	<i>economy</i>
InnerTest	Normalized fluctuations of the \mathbf{g}_n 's parallel components along $\mathbf{g}_{\mathcal{B}}$, proposed in [6]	<i>economy</i>
OrthoTest	Normalized fluctuations of the \mathbf{g}_n 's orthogonal components along $\mathbf{g}_{\mathcal{B}}$, proposed in [6]	<i>economy</i>
GradHist1d	Histogram of individual gradient elements, $\{\mathbf{g}_n(\theta_j)\}_{n \in \mathcal{B}, j=1, \dots, D}$	<i>economy</i>
TICDiag	Relation between (diagonal) curvature and gradient noise, inspired by [38]	<i>business</i>
HessTrace	Exact or approximate Hessian trace, $\text{Tr}(\mathbf{H}_{\mathcal{B}}(\theta))$, inspired by [44]	<i>business</i>
HessMaxEV	Maximum Hessian eigenvalue, $\lambda_{\max}(\mathbf{H}_{\mathcal{B}}(\theta))$, inspired by [44]	<i>full</i>
GradHist2d	Histogram of weights and individual gradient elements, $\{(\theta_j, \mathbf{g}_n(\theta_j))\}_{n \in \mathcal{B}, j=1, \dots, D}$	<i>full</i>

Table 1. **Overview of COCKPIT quantities.** They range from cheap byproducts, to nonlinear transformations of first-order information and Hessian-based measures. Some quantities have already been proposed, others are first to be considered in this work. They are categorized into configurations *economy* \leq *business* \leq *full* based on their run time overhead (see Section 4 for a detailed evaluation).

panel in Figure 2) distinguishes these two causes.

Gradient tests: How noisy is the batch? The batch size trades off gradient accuracy versus computational cost. Bolrapragada *et al.* [6] and Byrd *et al.* [8] proposed adaptive sampling strategies based on testing geometric constraints between mean and individual gradients. Their *norm*, *inner product*, and *orthogonality tests* use a standardized radius and two band widths (parallel and orthogonal to the gradient mean) that indicate how strongly individual gradients scatter around their mean. The original works use these values to adapt batch sizes. Instead, we use the standardized noise radius and band widths for visualization. COCKPIT combines all three gradient tests into a single instrument (top middle plot of Figure 2), which also monitors their evolution over time. These noise indicators can be used to guide batch size adaptation on- and offline, or to investigate the influence of gradient alignment on optimization speed [33] and generalization performance [9, 10, 24].

2.2. Hessian properties for local loss geometry

An intuition for the loss landscape's local geometry helps in many ways. It can help diagnose whether training is stuck, to adapt the step size, and can explain optimization stability or regularization [16, 20]. The principal challenge is the extreme weight-space dimension. Low-dimensional projections of high-dimensional surfaces can behave unintuitively [27], but tracking their most extreme or average behaviors may help in debugging, especially if first-order metrics fail.

Hessian eigenvalues: A gorge or a lake? In convex optimization, the maximum Hessian eigenvalue crucially determines the appropriate learning rate [34]. Many works have studied the Hessian spectrum in machine learning (*e.g.*,

[15, 16, 27, 31, 32, 44]). In short: curvature matters. Established [30] and recent advanced automatic differentiation frameworks [11] allow computing Hessian properties without computing the full matrix, and COCKPIT leverages this functionality to provide access to the the *Hessian's largest eigenvalue* and its *trace* (right top and middle plots in Figure 2). While the former corresponds to the loss surface's sharpest valley and can thus hint at optimization instabilities [20], a notion of “average curvature” is provided through the *Hessian trace*, since the eigenvalues λ_i relate to it by $\sum_i \lambda_i = \text{Tr}(\mathbf{H}_{\mathcal{B}}(\theta))$.

TIC: How do curvature and gradient noise interact? There is an ongoing debate about curvature's relationship to generalization (*e.g.*, [12, 19, 21, 38]). One recently proposed metric [38], the *Takeuchi Information criterion (TIC)* [37], estimates the generalization gap by a ratio between Hessian and non-central second gradient moment. It also provides intuition for changes in the objective function implied by gradient noise. Inspired by the approximations in [38], COCKPIT provides *mini-batch TIC estimates* during training (bottom right plot of Figure 2).

2.3. Visualizing internal network dynamics

Histograms are a natural visual compression of the high-dimensional individual gradients ($|\mathcal{B}| \times D$ numbers). They give insights into the gradient *distribution*, and hence provide a more detailed view of the learning signal, the gradient mean. In conjunction with the parameter associated to individual gradients, the entire model status (current parameter configuration and gradient distribution) and dynamics can be visualized in a single plot, and monitored during training. This provides a more fine-grained view of the model compared to tracking parameter and *gradient norm* [14].

Gradient and parameter-histograms: What is happening in our network? COCKPIT offers a univariate *histogram of the gradient elements* $\{g_n(\theta)_j\}_{n,j}$. Additionally, a combined *histogram of parameter-gradient pairs* $\{(\theta_j, g_n(\theta_j))\}_{n,j}$ provides a two-dimensional look into the frequencies of the network’s gradient and parameter values in a mini-batch. Both histograms are also able to show their data layer-wise. Section 3.1 shows an example use-case of the gradient histogram; Section 3.2 makes the case for layer-wise histograms.

3. Experiments

The diverse information provided by COCKPIT can help users and researchers in many ways, some of which, just like for a traditional debugger, only become apparent in practical use. In this section, we present a few motivating example applications, selecting specific instruments and scenarios in which these instruments are practically useful. Specifically, we first show COCKPIT can help the user discern between, and thus fix, common training bugs (Sections 3.1 and 3.2) that are otherwise hard to distinguish as they lead to the same failure: bad training. We demonstrate that COCKPIT can guide practitioners to choose efficient hyperparameters *within a single training run* (Sections 3.2 and 3.3). Finally, we highlight that COCKPIT’s instruments can provide research insights about the optimization process (Section 3.3). Our empirical findings are demonstrated on deep learning problems from the DEEPOBS [35] benchmark collection.

3.1. Incorrectly scaled data

One prominent source of bugs is the data pipeline. To pick a relatively simple example: For standard optimizers to work at the usual learning rates, inputs must be standardized (*i.e.* between zero and one, or have zero mean and unit variance [5, *e.g.*]). If the user forgets to do this, optimizer performance degrades (by how much depends on the original data scaling). It can be difficult to identify the source of this problem as it does not cause obvious failures, `NaN` or `Inf` gradients, *etc.*

We now construct a semi-realistic example, to show how using COCKPIT can help diagnose this problem upon observing slow training performance. By default¹, the popular image data sets CIFAR-10 and CIFAR-100 [22] are provided as NUMPy [18] arrays that consist of integers in the interval $[0, 255]$. This *raw* data, instead of the widely used version with floats in $[0, 1]$, changes the data scale by a factor of 255 (and thus the training gradients). Therefore, the optimizer’s optimal learning rate is scaled as well. In other words, the default parameters of popular optimization methods may not work well anymore, or good hyperparameters may take extreme values that are not discovered by a default parameter search.

¹<https://www.cs.toronto.edu/~kriz/cifar.html>

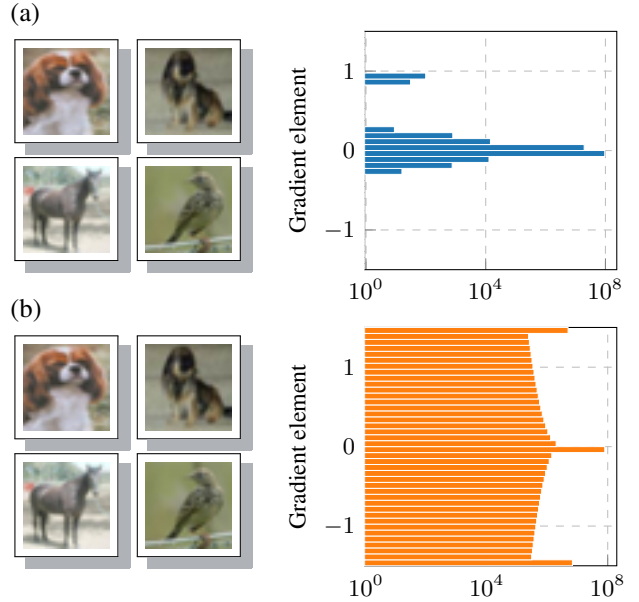


Figure 3. Same inputs, different gradients. Catching data processing bugs with COCKPIT. (a) normalized $[0, 1]$ and (b) raw $[0, 255]$ images look identical in auto-scaled front-ends like MATPLOTLIB’s `imshow`. The gradient distribution on the 3C3D architecture, however, is crucially affected by this scaling.

Even if the user directly inspects the training images, this may not be apparent (Figure 3). But the gradient histogram instrument of COCKPIT, which has a deliberate default plotting range around $[-1, 1]$ to highlight such problems, immediately and prominently shows that there is an issue.

Of course, this particular data is only a placeholder for real practical data sets. While this problem may not frequently arise in the highly pre-processed, packaged CIFAR-10, it is not a rare problem for practitioners who work with their personal data sets. This is particularly likely in domains outside standard computer vision, *e.g.* when working with mixed-variable data without obvious natural scale.

3.2. Vanishing gradients

The model architecture itself can be a source of training bugs. As before, such problems mostly arise with novel data sets, where well-working architectures are unknown. The following example shows how even small (in terms of code) architecture modifications may severely harm the training.

Figure 4 (a) shows the distribution of gradient values of two different network architectures in blue and orange. Although the blue network trains considerably better than the orange one, their gradient distributions look quite similar. The difference becomes evident when inspecting the gradient histogram *layer-wise*. We can see that many layers have a degenerated gradient distribution. Many elements are practically zero (see Figure 4 (b), bottom row). Since the last fully-connected layers have many more parameters (a

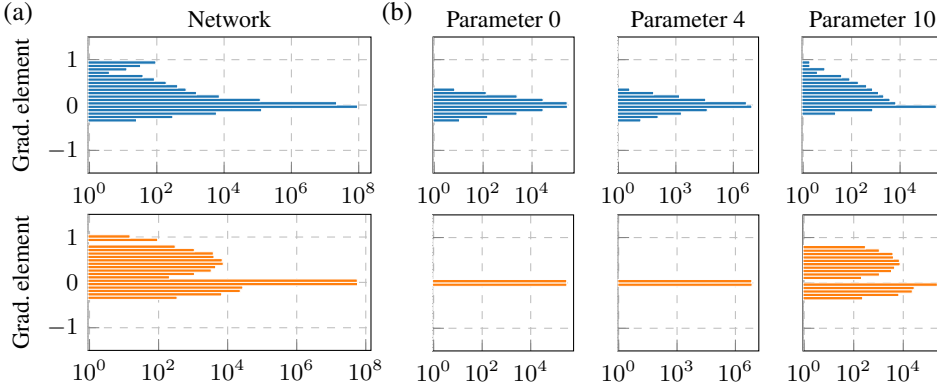


Figure 4. **Gradient distributions of two similar architectures on the same problem.** (a) Distribution of individual gradient elements summarized over the entire network. Both seem similar. (b) Layer-wise histograms for a subset of layers. Parameter 0 is the layer closest to the network’s input, parameter 10 closest to its output. Only the layer-wise view reveals significant differences.

classic pattern many convolutional neural nets follow), they dominate the network-wide histogram. This obscures that a considerable network part is effectively unable to train.

Both the blue and orange networks follow DEEPOBS’s 3C3D architecture. The only difference is the non-linearity: The blue network uses standard ReLU activations, while the orange one has sigmoid activations. Here, the layer-wise histogram instrument of COCKPIT highlights which part of the architecture makes training unnecessarily hard. Accessing information layer-wise is also essential due to the strong overparameterization in deep models where training can happen in small subspaces [17]. Once again, this is hard to do with common monitoring tools, such as the loss curve.

3.3. Tuning learning rates

Once the architecture is defined, the optimizer’s learning rate is the most important hyperparameter to tune. Getting it right requires extensive hyperparameter searches at high resource costs. COCKPIT’s instruments can provide intuition and information to streamline this process: In contrast to the raw learning rate, the curvature-standardized step-size α -quantity (Section 2.1) has a natural scale.

Across multiple optimization problems, we observe, perhaps surprisingly, that the best runs and indeed all good runs have a mean $\alpha > 0$ (Figure 5). This experiment illustrates a fundamental difference between the stochastic optimization typical of contemporary machine learning and classic deterministic optimization tasks. Instead of locally stepping “to the valley floor” (which is optimal in the deterministic case), stochastic optimizers should *overshoot* the valley somewhat. This necessity to “surf the walls” has been reported before (e.g. [42, 43]) as a property of neural network training.

Figure 5 also indicates a major challenge preventing simple automated tuning solutions: The optimal α -value is problem-dependent, and simpler problems, such as a multi-layer perceptron (MLP) on MNIST [23], behave more similarly to classic optimization problems. Algorithmic research on small problems can thus produce misleading conclusions.

Learning rates are also frequently adapted during training.

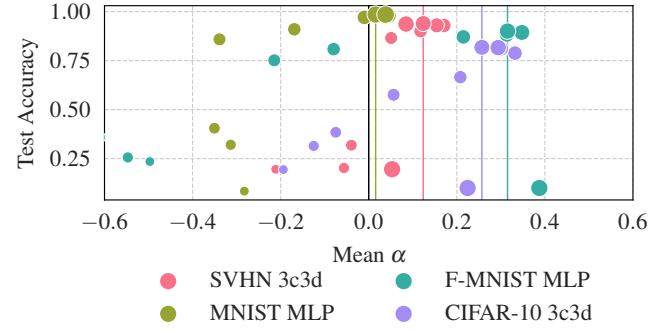


Figure 5. **Final test accuracy as a function of standardized step-size α .** For multiple test problems, final test accuracy is shown against average α -value over the whole training period. Marker size indicates the magnitude of the raw learning rate used, marker color identifies tasks (legend below). For each problem, the best-performing setting is highlighted by a vertical colored line.

This fits with the observation above about positive α -values. “Overshooting” allows fast early progression towards areas of lower loss, but it does of course not yield convergence in the end. This kind of fine-tuning requires online, real-time visualization of the training state, as is possible in COCKPIT.

Figure 5 shows that the α -gauge is not sufficient by itself: extreme overshooting with a too large learning rate leads to poor performance, which however can be prevented by taking additional instruments into account. This makes the case for the cockpit-metaphor of monitoring several instruments in conjunction. By combining the α -instrument with other gauges that capture the local geometry or network dynamics, the user can better identify good choices of the learning rate and other hyperparameters.

4. Benchmark

The previous section made a case for COCKPIT as an effective debugging and tuning tool. To make the library useful in a practical online setting, it must also have limited computational cost. We now show that it is possible to compute all the necessary quantities at reasonable computational overhead. The user can control the absolute cost along two

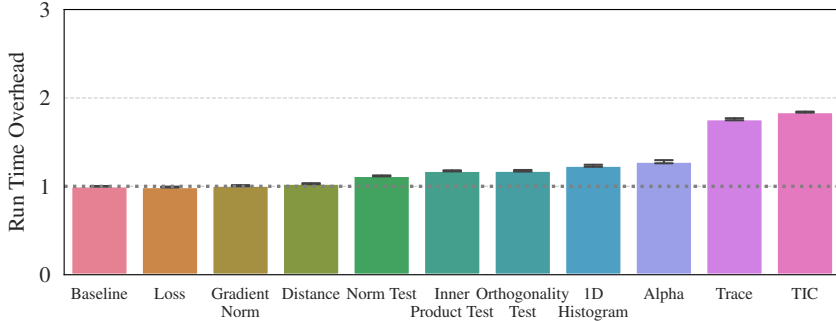


Figure 6. **Run time overhead for individual COCKPIT instruments on a GPU.** Run times on CIFAR-10 3C3D are shown as multiples of the *baseline* (no tracking). Most instruments add little overhead. This plot shows the overhead for computations in one iteration, determined by averaging over multiple iterations and random seeds. By reducing the tracking interval, the relative overhead across the full training process can be made orders of magnitude smaller (Figure 7).

dimensions, by reducing the number of instruments shown, or by reducing their update frequency.

Complexity analysis/expected performance: Computing more information introduces computational overhead, of course. However, recent work [11] has demonstrated that first-order information, like distributional statistics on the batch gradients, can be computed on top of the mean gradient at little extra cost. Similar savings apply for most other quantities listed in Table 1, as they are (non-)linear transformations of individual gradients.

A subset of COCKPIT quantities uses second-order information from the Hessian diagonal. For ReLU networks on a classification task with C classes, the additional work is proportional to C gradient backpropagations (*i.e.* $C = 10$ for CIFAR-10, $C = 100$ for CIFAR-100). Parallel processing can, to some extent, process these extra backpropagations in parallel without significant overhead. If this is no longer possible, we can fall back to a Monte Carlo (MC) sampling approximation, which reduces the number of extra backprop passes to the number of samples (1 by default).²

While parallelization is possible for the gradient instruments, computing the maximum Hessian eigenvalue is inherently sequential. Similar to [44], we use matrix-free Hessian-vector products by automatic differentiation [30], where each product has a cost proportional to one gradient computation. Regardless of the underlying iterative eigensolver, multiple such products must be queried to compute the spectral norm (the required number depends on the spectral gap to the second-largest eigenvalue). This step is thus costly and introduces the largest computational overhead.

Run time benchmark: Figure 6 shows the wall-clock computational overhead for individual instruments. These times were collected on a GPU for the CIFAR-10 3C3D test problem (details in Appendix C).³ As expected, byproducts

²Indeed, such an MC-sampled approximation of the Hessian/generalized Gauss-Newton has been used in Figure 2 to reduce the prohibitively large number of extra backpropagations on CIFAR-100 ($C = 100$).

³We do not show run times for HessMaxEV because the associated overhead is large compared to the other quantities, as described above. Surprisingly, we observed significant cost for the two-dimensional histogram

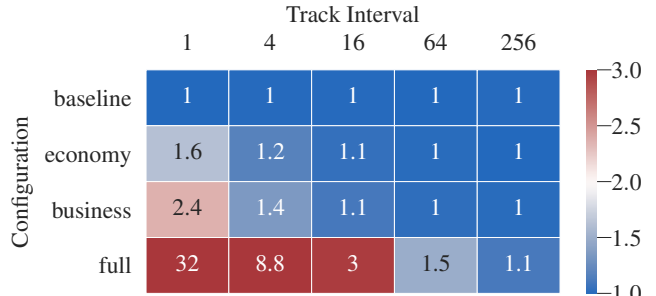


Figure 7. **Overhead of different COCKPIT configurations for varying tracking intervals.** Results collected while training on CIFAR-10 3C3D on a GPU. Blue fields mark settings which allow tracking without doubling the training time. More in Appendix C.2.

are virtually free, and quantities that rely solely on first-order information add a small overhead (at most roughly 25 % on this particular problem). Thanks to parallelization, the 10 extra backward passes required for Hessian quantities reduce to a less than 100 % overhead. As we will see now, the individual overheads also do not simply add up when multiple quantities are tracked, because quantities relying on the same information share computations.

To allow a rough cost control, COCKPIT currently offers three configurations, called *economy*, *business*, and *full*, in increasing order of cost (cf. Table 1). As a rough guideline, we consider a factor of two to be an acceptable limit for the increase in training time and benchmark the configurations’ run times for different tracking intervals. Figure 7 shows a performance matrix for the CIFAR-10 3C3D problem, where settings that meet this limit are set in blue.

Improved performance due to shared computations is easy to read off from this figure: Summing all the individual overheads shown in Figure 6 would result in a total overhead larger than 200 %, while the joint overhead (*business*) reduces to 140 %. The *economy* configuration can easily be tracked at every step of this problem and stay well below our threshold of doubling the execution time. COCKPIT’s

on GPU. It is caused by an implementation bottleneck for histogram shapes observed in deep models. We thus also omit the run time of GradHist2d here, as we expect it to be eliminated with future implementations (see Appendix C.2 for a detailed performance analysis and additional benchmarks).

view shown in Figure 2 can be updated every 64-th iteration without a major increase in training time (this corresponds to about five updates per epoch). Finally, tracking any configuration about once per epoch – which is what many practitioners do – adds overhead close to zero (rightmost column).

This good performance is largely due to the efficiency of the BACKPACK package, which we leverage with custom and optimized modification, that compacts information layer-wise and then discards unneeded buffers. Using layer-wise information (Section 3.2) scales better to large networks, where storing the entire model’s individual gradients all at once becomes increasingly expensive (see Appendix C).

To the best of our knowledge, many of the quantities in Table 1, especially those relying on individual gradients, have only been explored on rather small problems. With COCKPIT they can now be accessed at a reasonable rate for deep learning models outside the toy problem category.

5. Showcase

Having introduced and benchmarked the tool, we can now return to Figure 2 for a closer look. The figure shows a snapshot from training the ALL-CNN-C [36] on CIFAR-100 using SGD with a restarted cyclic learning rate schedule (see bottom left panel). Diagonal curvature instruments are configured to use an MC approximation in order to reduce the run time (remember that $C = 100$ here, compare Section 4).

A glance at all panels shows that the learning rate schedule is reflected in the metrics. However, the instruments also reveal interesting behavior in the early phase of training (first ~ 100 iterations), where the learning rate is still unaffected by the schedule: There, the loss plateaus and the optimizer takes relatively small steps (compared to later, as can be seen in the small gradient norms, and small distance from initialization). Based on these low-cost instruments, one may thus at first suspect that training was poorly initialized; but training indeed succeeds after iteration 100! Viewing COCKPIT entirely though, it becomes clear that optimization is not stuck at all: While loss, gradient norms and distance in parameter space remain almost constant, curvature changes, which expresses itself in a clear downward trend of the maximum Hessian eigenvalue (top right panel).

The importance of early phases in deep learning has recently been hypothesized in [14], suggesting a logarithmic timeline. Not only does our showcase support this hypothesis, it also adds evidence through the curvature-based metrics, which in this particular case are the only meaningful feedback in the first few training steps. It also suggests that training should be monitored at log-spaced intervals. COCKPIT provides the flexibility to do so, indeed, Figure 2 has been created with log-scheduled tracking events.

As a final note, we acknowledge that the approach taken here promotes an amount of “manual” work (monitoring metrics, taking decisions to intervene, *etc.*) that may seem

ironic, at odds with the paradigm of automation that is at the heart of machine learning. While we recognize this problem, we argue that it is what is needed at this point in the development of the field. Deep learning has to a large extent been driven by scaling computational resources [39], and fully-automated, one-shot training may still be some way out. To develop better optimization algorithms, researchers, not just users, need more direct insights and intuition about the processes taking place “inside” neural networks. We argue that the tool presented in this work provides just that.

To highlight how this may work, in Appendix D, we show the COCKPIT view of two convex DEEPOBS problems: a noisy quadratic and logistic regression on MNIST. For these problems, the instruments behave quite differently compared to the deep learning problem in Figure 2. In particular, the gradient norm increases (left column, bottom panel) over training, and individual gradients become less scattered (center column, top panel). This is diametrically opposed to the convex problems and shows that deep learning differs even quantitatively from well-understood optimization problems.

6. Conclusion

In contrast to classic deterministic optimization problems, contemporary machine learning, in particular deep learning, remains a craft and an art. High dimensionality, stochasticity, and non-convexity require constant tracking and tuning, often resulting in a painful process of trial and error. When things fail, popular performance measures, like the training loss, do not provide enough information by themselves. These metrics only tell *whether* the model is learning, but not *why*. Alternatively, traditional debugging tools can provide access to individual weights and data. However, in models whose power only arises from the statistical properties of myriad weights, this approach is hopeless, like looking for the proverbial needle in a haystack.

To alleviate this problem, we proposed COCKPIT, a visual and practical debugging tool for deep learning. It offers instruments to monitor the network’s internal dynamics during optimization, in real-time. Although these instruments utilize rich second-order information, efficient computation keeps the necessary runtime overhead reasonable.

To demonstrate the tool’s utility, we showed how it can identify bugs where traditional tools fail. The whole software package is available for PYTORCH, can be added to many existing training loops, and will be released as open source.

Of course, such a tool is never complete. Just like there is no perfect universal debugger, the list of currently implemented instruments is necessarily incomplete. However, our experiments show that COCKPIT provides useful tools and extracts valuable information not currently otherwise available to the user. We believe that this information can help practitioners to simply make their architectures work, but also inspire researchers to build new intuitions for how

to improve optimization. The source code is structured flexibly, such that new instruments can be added easily without changing the internals. Computational layer and graphical front-end are separated, so users who prefer other tools, *e.g.* TENSORBOARD, can pipe them there, too. And of course, instead of just displaying the information, the same numbers can also be used by novel algorithms directly, side-stepping the human in the loop.

Acknowledgments

The authors gratefully acknowledge financial support by the European Research Council through ERC StG Action 757275 / PANAMA; the DFG Cluster of Excellence “Machine Learning - New Perspectives for Science”, EXC 2064/1, project number 390727645; the German Federal Ministry of Education and Research (BMBF) through the Tübingen AI Center (FKZ: 01IS18039A); and funds from the Ministry of Science, Research and Arts of the State of Baden-Württemberg. Moreover, the authors thank the International Max Planck Research School for Intelligent Systems (IMPRS-IS) for supporting Felix Dangel and Frank Schneider. Further, we are grateful to Agustinus Kristiadi, Alexandra Gessner, Christian Fröhlich, Filip de Roos, Jonathan Wenger, Julia Grosse, Lukas Tatzel, Marius Hobbahn, and Nicholas Krämer for providing feedback to the manuscript.

References

- [1] Martín Abadi, Ashish Agarwal, Paul Barham, Eugene Brevdo, Zhifeng Chen, Craig Citro, Greg S. Corrado, Andy Davis, Jeffrey Dean, Matthieu Devin, Sanjay Ghemawat, Ian Goodfellow, Andrew Harp, Geoffrey Irving, Michael Isard, Yangqing Jia, Rafal Jozefowicz, Lukasz Kaiser, Manjunath Kudlur, Josh Levenberg, Dandelion Mané, Rajat Monga, Sherry Moore, Derek Murray, Chris Olah, Mike Schuster, Jonathon Shlens, Benoit Steiner, Ilya Sutskever, Kunal Talwar, Paul Tucker, Vincent Vanhoucke, Vijay Vasudevan, Fernanda Viégas, Oriol Vinyals, Pete Warden, Martin Wattenberg, Martin Wicke, Yuan Yu, and Xiaoqiang Zheng. TensorFlow: Large-scale machine learning on heterogeneous systems, 2015. Software available from tensorflow.org. [1](#)
- [2] Ayush Manish Agrawal, Atharva Tendle, Harshvardhan Sikka, Sahib Singh, and Amr Kayid. Investigating learning in deep neural networks using layer-wise weight change, 2020. [3](#)
- [3] Achraf Bahamou and Donald Goldfarb. A dynamic sampling adaptive-SGD method for machine learning, 2019. [18](#)
- [4] Lukas Balles, Javier Romero, and Philipp Hennig. Coupling adaptive batch sizes with learning rates, 2017. [2, 11, 14](#)
- [5] Yoshua Bengio. Practical recommendations for gradient-based training of deep architectures, 2012. [5](#)
- [6] Raghu Bollapragada, Richard H. Byrd, and Jorge Nocedal. Adaptive sampling strategies for stochastic optimization. *SIAM Journal on Optimization*, 28:3312–3343, 2017. [4, 11, 15, 16, 17, 18](#)
- [7] James Bradbury, Roy Frostig, Peter Hawkins, Matthew James Johnson, Chris Leary, Dougal Maclaurin, and Skye Wanderman-Milne. JAX: composable transformations of Python+NumPy programs, 2018. [2](#)
- [8] Richard H. Byrd, Gillian M. Chin, Jorge Nocedal, and Yuchen Wu. Sample size selection in optimization methods for machine learning. *Math. Program.*, 134(1):127–155, 2012. [4, 11, 15, 16](#)
- [9] Satrajit Chatterjee. Coherent gradients: An approach to understanding generalization in gradient descent-based optimization. In *International Conference on Learning Representations*, 2020. [4](#)
- [10] Satrajit Chatterjee and Piotr Zielinski. Making coherence out of nothing at all: Measuring the evolution of gradient alignment, 2020. [4](#)
- [11] Felix Dangel, Frederik Kunstner, and Philipp Hennig. BackPACK: Packing more into backprop. In *International Conference on Learning Representations*, 2020. [1, 2, 4, 7](#)
- [12] Laurent Dinh, Razvan Pascanu, Samy Bengio, and Yoshua Bengio. Sharp minima can generalize for deep nets. In Doina Precup and Yee Whye Teh, editors, *Proceedings of the 34th International Conference on Machine Learning, ICML 2017, Sydney, NSW, Australia, 6-11 August 2017*, volume 70 of *Proceedings of Machine Learning Research*, pages 1019–1028. PMLR, 2017. [4](#)
- [13] Fartash Faghri, David Duvenaud, David J. Fleet, and Jimmy Ba. A study of gradient variance in deep learning, 2020. [2](#)
- [14] Jonathan Frankle, David J. Schwab, and Ari S. Morcos. The early phase of neural network training, 2020. [3, 4, 8](#)

[15] Behrooz Ghorbani, Shankar Krishnan, and Ying Xiao. An investigation into neural net optimization via Hessian eigenvalue density, 2019. 4

[16] Boris Ginsburg. On regularization of gradient descent, layer imbalance and flat minima, 2020. 4

[17] Guy Gur-Ari, Daniel A. Roberts, and Ethan Dyer. Gradient descent happens in a tiny subspace, 2019. 6

[18] Charles R. Harris, K. Jarrod Millman, Stéfan J. van der Walt, Ralf Gommers, Pauli Virtanen, David Cournapeau, Eric Wieser, Julian Taylor, Sebastian Berg, Nathaniel J. Smith, Robert Kern, Matti Picus, Stephan Hoyer, Marten H. van Kerkwijk, Matthew Brett, Allan Haldane, Jaime Fernández del Río, Mark Wiebe, Pearu Peterson, Pierre Gérard-Marchant, Kevin Sheppard, Tyler Reddy, Warren Weckesser, Hameer Abbasi, Christoph Gohlke, and Travis E. Oliphant. Array programming with NumPy. *Nature*, 585(7825):357–362, Sept. 2020. 5

[19] Sepp Hochreiter and Jürgen Schmidhuber. Flat minima. *Neural Comput.*, 9(1):1–42, 1997. 4

[20] Stanislaw Jastrzebski, Maciej Szymczak, Stanislav Fort, Devansh Arpit, Jacek Tabor, Kyunghyun Cho, and Krzysztof Geras. The break-even point on optimization trajectories of deep neural networks. In *International Conference on Learning Representations*, 2020. 4

[21] Nitish Shirish Keskar, Dheevatsa Mudigere, Jorge Nocedal, Mikhail Smelyanskiy, and Ping Tak Peter Tang. On large-batch training for deep learning: Generalization gap and sharp minima. In *5th International Conference on Learning Representations, ICLR 2017, Toulon, France, April 24-26, 2017, Conference Track Proceedings*. OpenReview.net, 2017. 4

[22] Alex Krizhevsky. Learning multiple layers of features from tiny images. Technical report, 2009. 5

[23] Yann Lecun, Léon Bottou, Yoshua Bengio, and Patrick Haffner. Gradient-based learning applied to document recognition. In *Proceedings of the IEEE*, volume 86, pages 2278–2324, 1998. 6

[24] Jinlong Liu, Yunzhi Bai, Guoqing Jiang, Ting Chen, and Huayan Wang. Understanding why neural networks generalize well through GSNR of parameters. In *International Conference on Learning Representations*, 2020. 2, 4, 11, 19

[25] Maren Mahsereci, Lukas Balles, Christoph Lassner, and Philipp Hennig. Early stopping without a validation set, 2017. 2, 11, 15

[26] Maren Mahsereci and Philipp Hennig. Probabilistic line searches for stochastic optimization. In *Advances in Neural Information Processing Systems*, volume 28, 2015. 14

[27] Rotem Mulayoff and Tomer Michaeli. Unique properties of flat minima in deep networks, 2020. 4

[28] Vaishnavh Nagarajan and J. Zico Kolter. Generalization in deep networks: The role of distance from initialization, 2019. 3

[29] Adam Paszke, Sam Gross, Francisco Massa, Adam Lerer, James Bradbury, Gregory Chanan, Trevor Killeen, Zeming Lin, Natalia Gimelshein, Luca Antiga, Alban Desmaison, Andreas Kopf, Edward Yang, Zachary DeVito, Martin Raison, Alykhan Tejani, Sasank Chilamkurthy, Benoit Steiner, Lu Fang, Junjie Bai, and Soumith Chintala. Pytorch: An imperative style, high-performance deep learning library. In H. Wallach, H. Larochelle, A. Beygelzimer, F. d' Alché-Buc, E. Fox, and R. Garnett, editors, *Advances in Neural Information Processing Systems 32*, pages 8024–8035. Curran Associates, Inc., 2019. 1

[30] Barak A. Pearlmutter. Fast exact multiplication by the Hessian. *Neural Computation*, 6(1):147–160, 1994. 4, 7, 18

[31] Levent Sagun, Leon Bottou, and Yann LeCun. Eigenvalues of the Hessian in deep learning: Singularity and beyond, 2017. 4

[32] Levent Sagun, Utku Evci, V. Ugur Guney, Yann Dauphin, and Leon Bottou. Empirical analysis of the Hessian of overparametrized neural networks, 2018. 4

[33] Karthik A. Sankararaman, Soham De, Zheng Xu, W. Ronny Huang, and Tom Goldstein. The impact of neural network overparameterization on gradient confusion and stochastic gradient descent, 2019. 4

[34] Mark Schmidt. Convergence rate of stochastic gradient with constant step size, 2014. 4

[35] Frank Schneider, Lukas Balles, and Philipp Hennig. Deep-OBS: A Deep Learning Optimizer Benchmark Suite. In *7th International Conference on Learning Representations, ICLR*, mar 2019. 5

[36] Jost Tobias Springenberg, Alexey Dosovitskiy, Thomas Brox, and Martin Riedmiller. Striving for simplicity: The all convolutional net, 2015. 3, 8

[37] Kei Takeuchi. The distribution of information statistics and the criterion of goodness of fit of models. *Mathematical Science*, 153:12–18, 1976. 4, 18

[38] Valentin Thomas, Fabian Pedregosa, Bart van Merriënboer, Pierre-Antoine Mangazol, Yoshua Bengio, and Nicolas Le Roux. On the interplay between noise and curvature and its effect on optimization and generalization, 2019. 4, 11, 18, 19

[39] Neil C. Thompson, Kristjan Greenewald, Keeheon Lee, and Gabriel F. Manso. The computational limits of deep learning, 2020. 8

[40] Sharan Vaswani, Aaron Mishkin, Issam Laradji, Mark Schmidt, Gauthier Gidel, and Simon Lacoste-Julien. Painless stochastic gradient: Interpolation, line-search, and convergence rates. In *Advances in Neural Information Processing Systems*, volume 32, 2019. 14

[41] James Warsa, Todd Wareing, Jim Morel, John McGhee, and Richard Lehoucq. Krylov subspace iterations for deterministic k-eigenvalue calculations. *Nuclear Science and Engineering - NUCL SCI ENG*, 147, 05 2004. 18

[42] Yuhuai Wu, Mengye Ren, Renjie Liao, and Roger B. Grosse. Understanding short-horizon bias in stochastic meta-optimization. *6th International Conference on Learning Representations, ICLR 2018 - Conference Track Proceedings*, mar 2018. 6

[43] Chen Xing, Devansh Arpit, Christos Tsirigotis, and Yoshua Bengio. A Walk with SGD, 2018. 6, 14

[44] Zhewei Yao, Amir Gholami, Kurt Keutzer, and Michael Mahoney. PyHessian: Neural networks through the lens of the Hessian, 2019. 4, 7, 11, 18

A. COCKPIT instruments overview

Table 2 lists all quantities available in the first public release of COCKPIT. If necessary, we provide references to their mathematical definition. This table contains additional quantities, compared to Table 1 in the main text. To improve the presentation of this work, we decided to not describe every quantity available in COCKPIT in the main part and instead focus on the investigated metrics. Custom quantities can be added easily without having to understand the inner-workings.

Name	Description	Math
Loss	Mini-batch loss at current iteration, $\mathcal{L}_{\mathcal{B}}(\boldsymbol{\theta})$	(1)
Parameters	Parameter values $\boldsymbol{\theta}_t$ at the current iteration	-
Distance	Update size $\ \boldsymbol{\theta}_{t+1} - \boldsymbol{\theta}_t\ $ and distance from initialization $\ \boldsymbol{\theta}_t - \boldsymbol{\theta}_0\ $	-
GradNorm	Mini-batch gradient norm $\ \mathbf{g}_{\mathcal{B}}(\boldsymbol{\theta})\ $	-
Time	Time of the current iteration (e.g. used in benchmark of Appendix C)	-
Alpha	Normalized step on a noisy quadratic interpolation between two iterates $\boldsymbol{\theta}_t, \boldsymbol{\theta}_{t+1}$	(10)
CABS	Adaptive batch size for SGD, optimizes expected objective gain per cost, from [4]	(12)
EarlyStopping	Evidence-based early stopping criterion for SGD, proposed in [25]	(14d)
GradHist1d	Histogram of individual gradient elements, $\{\mathbf{g}_n(\boldsymbol{\theta}_j)\}_{n \in \mathcal{B}, j=1, \dots, D}$	(15)
GradHist2d	Histogram of weights and individual gradient elements, $\{(\boldsymbol{\theta}_j, \mathbf{g}_n(\boldsymbol{\theta}_j))\}_{n \in \mathcal{B}, j=1, \dots, D}$	(16)
NormTest	Normalized fluctuations of the residual norms $\ \mathbf{g}_{\mathcal{B}} - \mathbf{g}_n\ $, proposed in [8]	(19c)
InnerTest	Normalized fluctuations of the \mathbf{g}_n 's parallel components along $\mathbf{g}_{\mathcal{B}}$, proposed in [6]	(22c)
OrthoTest	Normalized fluctuations of the \mathbf{g}_n 's orthogonal components along $\mathbf{g}_{\mathcal{B}}$, proposed in [6]	(25b)
HessMaxEV	Maximum Hessian eigenvalue, $\lambda_{\max}(\mathbf{H}_{\mathcal{B}}(\boldsymbol{\theta}))$, inspired by [44]	(26)
HessTrace	Exact or approximate Hessian trace, $\text{Tr}(\mathbf{H}_{\mathcal{B}}(\boldsymbol{\theta}))$, inspired by [44]	-
TICDiag	Relation between (diagonal) curvature and gradient noise, inspired by [38]	(29)
TICTrace	Relation between curvature and gradient noise trace, inspired by [38]	(28)
MeanGSNR	Average gradient signal-to-noise-ratio (GSNR), inspired by [24]	(31b)

Table 2. **Overview of all COCKPIT quantities** with a short description and, if necessary, a reference to mathematical definition.

B. Mathematical details

In this section, we want to provide the mathematical background for each instrument described in Table 2. This complements the more informal description presented in Section 2 in the main text, which focused more on the expressiveness of the individual quantities. We will start by setting up the necessary notation in addition to the one introduced in Section 2.

B.1. Additional notation

Population properties: The population risk $\mathcal{L}_P(\boldsymbol{\theta}) \in \mathbb{R}$ and its variance $\Lambda(\boldsymbol{\theta}) \in \mathbb{R}$ are given by

$$\mathcal{L}_P(\boldsymbol{\theta}) = \mathbb{E}_{(\mathbf{x}, \mathbf{y}) \sim P} [\ell(f(\boldsymbol{\theta}, \mathbf{x}), \mathbf{y})] = \int \ell(f(\boldsymbol{\theta}, \mathbf{x}), \mathbf{y}) P(\mathbf{x}, \mathbf{y}) d\mathbf{x} d\mathbf{y}, \quad (4a)$$

$$\Lambda_P(\boldsymbol{\theta}) = \text{Var}_{(\mathbf{x}, \mathbf{y}) \sim P} [\ell(f(\boldsymbol{\theta}, \mathbf{x}), \mathbf{y})] = \int (\ell(f(\boldsymbol{\theta}, \mathbf{x}), \mathbf{y}) - \mathcal{L}_P(\boldsymbol{\theta}))^2 P(\mathbf{x}, \mathbf{y}) d\mathbf{x} d\mathbf{y}. \quad (4b)$$

The population gradient $\mathbf{g}_P(\boldsymbol{\theta}) \in \mathbb{R}^D$ and its variance $\boldsymbol{\Sigma}_P(\boldsymbol{\theta}) \in \mathbb{R}^{D \times D}$ are given by

$$\mathbf{g}_P(\boldsymbol{\theta}) = \mathbb{E}_{(\mathbf{x}, \mathbf{y}) \sim P} [\nabla_{\boldsymbol{\theta}} \ell(f(\boldsymbol{\theta}, \mathbf{x}), \mathbf{y})] = \int \nabla_{\boldsymbol{\theta}} \ell(f(\boldsymbol{\theta}, \mathbf{x}), \mathbf{y}) P(\mathbf{x}, \mathbf{y}) d\mathbf{x} d\mathbf{y}, \quad (5a)$$

$$\begin{aligned} \boldsymbol{\Sigma}_P(\boldsymbol{\theta}) &= \text{Var}_{(\mathbf{x}, \mathbf{y}) \sim P} [\nabla_{\boldsymbol{\theta}} \ell(f(\boldsymbol{\theta}, \mathbf{x}), \mathbf{y})] \\ &= \int (\nabla_{\boldsymbol{\theta}} \ell(f(\boldsymbol{\theta}, \mathbf{x}), \mathbf{y}) - \mathbf{g}_P(\boldsymbol{\theta})) (\nabla_{\boldsymbol{\theta}} \ell(f(\boldsymbol{\theta}, \mathbf{x}), \mathbf{y}) - \mathbf{g}_P(\boldsymbol{\theta}))^\top P(\mathbf{x}, \mathbf{y}) d\mathbf{x} d\mathbf{y}. \end{aligned} \quad (5b)$$

Empirical approximations: Let \mathcal{S} denote a set of samples drawn i.i.d. from P , i.e. $\mathcal{S} = \{(\mathbf{x}_i, \mathbf{y}_i) \mid i = 1, \dots, |\mathcal{S}|\}$. With a slight abuse of notation the empirical risk approximated with \mathcal{S} is

$$\mathcal{L}_{\mathcal{S}}(\boldsymbol{\theta}) = \frac{1}{|\mathcal{S}|} \sum_{n \in \mathcal{S}} \ell_n(\boldsymbol{\theta}) \quad (6a)$$

(later, \mathcal{S} will represent either a mini-batch \mathcal{B} , or the train set \mathcal{D}). The empirical risk gradient $\mathbf{g}_{\mathcal{S}}(\boldsymbol{\theta}) \in \mathbb{R}^D$ on \mathcal{S} is

$$\mathbf{g}_{\mathcal{S}}(\boldsymbol{\theta}) = \nabla_{\boldsymbol{\theta}} \mathcal{L}_{\mathcal{S}}(\boldsymbol{\theta}) = \frac{1}{|\mathcal{S}|} \sum_{n \in \mathcal{S}} \nabla_{\boldsymbol{\theta}} \ell_n(\boldsymbol{\theta}) = \frac{1}{|\mathcal{S}|} \sum_{n \in \mathcal{S}} \mathbf{g}_n(\boldsymbol{\theta}), \quad (6b)$$

with individual gradients $\mathbf{g}_n(\boldsymbol{\theta}) = \nabla_{\boldsymbol{\theta}} \ell_n(\boldsymbol{\theta}) \in \mathbb{R}^D$ implied by a sample n . Population risk and gradient variances $\Lambda_P(\boldsymbol{\theta}), \boldsymbol{\Sigma}_P(\boldsymbol{\theta})$ can be empirically estimated on \mathcal{S} with the sample variances $\hat{\Lambda}_{\mathcal{S}}(\boldsymbol{\theta}) \in \mathbb{R}$, $\hat{\boldsymbol{\Sigma}}_{\mathcal{S}}(\boldsymbol{\theta}) \in \mathbb{R}^{D \times D}$, given by

$$\Lambda_P(\boldsymbol{\theta}) \approx \frac{1}{|\mathcal{S}| - 1} \sum_{n \in \mathcal{S}} (\ell_n(\boldsymbol{\theta}) - \mathcal{L}_{\mathcal{S}}(\boldsymbol{\theta}))^2 := \hat{\Lambda}_{\mathcal{S}}(\boldsymbol{\theta}), \quad (7a)$$

$$\begin{aligned} \boldsymbol{\Sigma}_P(\boldsymbol{\theta}) &\approx \frac{1}{|\mathcal{S}| - 1} \sum_{n \in \mathcal{S}} (\mathbf{g}_n(\boldsymbol{\theta}) - \mathbf{g}_{\mathcal{S}}(\boldsymbol{\theta})) (\mathbf{g}_n(\boldsymbol{\theta}) - \mathbf{g}_{\mathcal{S}}(\boldsymbol{\theta}))^\top := \hat{\boldsymbol{\Sigma}}_{\mathcal{S}}(\boldsymbol{\theta}) \\ &\approx \frac{1}{|\mathcal{S}| - 1} \left[\left(\sum_{n \in \mathcal{S}} \mathbf{g}_n(\boldsymbol{\theta}) \mathbf{g}_n(\boldsymbol{\theta})^\top \right) - |\mathcal{S}| \mathbf{g}_{\mathcal{S}}(\boldsymbol{\theta}) \mathbf{g}_{\mathcal{S}}(\boldsymbol{\theta})^\top \right]. \end{aligned} \quad (7b)$$

Often, gradient elements are assumed independent and hence their variance is diagonal (\odot^2 denotes element-wise square),

$$\text{diag}(\boldsymbol{\Sigma}_P(\boldsymbol{\theta})) \approx \frac{1}{|\mathcal{S}| - 1} \sum_{n \in \mathcal{S}} (\mathbf{g}_n(\boldsymbol{\theta}) - \mathbf{g}_{\mathcal{S}}(\boldsymbol{\theta}))^{\odot 2} = \text{diag}(\hat{\boldsymbol{\Sigma}}_{\mathcal{S}}(\boldsymbol{\theta})) \in \mathbb{R}^D. \quad (8)$$

Slicing: To avoid confusion between $\boldsymbol{\theta}_t$ (parameter at iteration t) and $\boldsymbol{\theta}_j$ (j -th parameter entry), we denote the latter as $[\boldsymbol{\theta}]_j$.

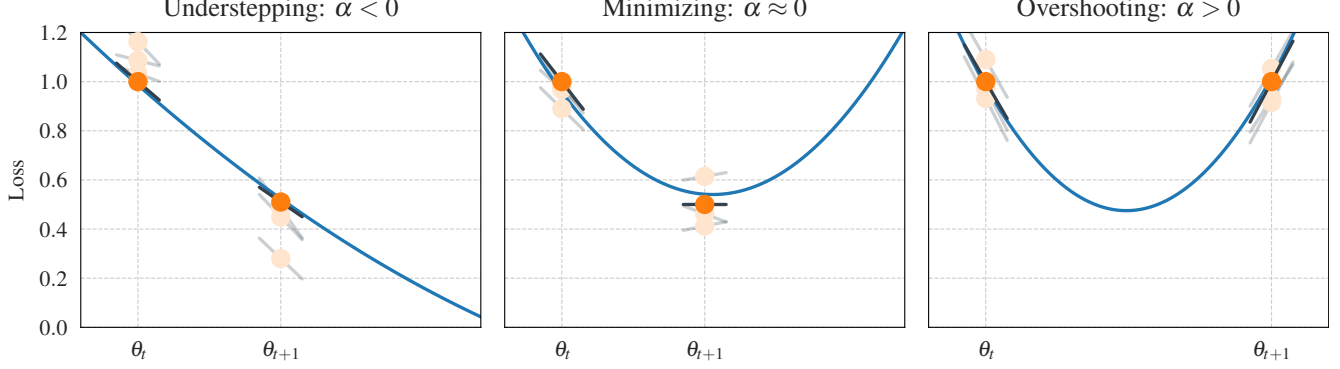


Figure 8. **Motivational sketch for the α quantity.** In each iteration of the optimizer we observe the loss function at two positions θ_t and θ_{t+1} (shown in \bullet). The black lines (—) show the observed slope at this position, which we can get from projecting the gradients onto the current step direction $\theta_{t+1} - \theta_t$. Note, that all four observations (two loss and two slope values) are noisy, due to being computed on a mini-batch. With access to the individual losses and gradients (some samples shown in \bullet /—), we can estimate their noise level and build a noise-informed quadratic fit (—). Using this fit, we determine whether the optimizer minimizes the local univariate loss (*middle plot*), or whether we understep (*left plot*) or overshoot (*right plot*) the minimum.

B.2. Alpha (AlphaOptimized, AlphaGeneral)

Motivation: The goal of the α -quantity is to estimate and quantify the effect that a selected learning rate has on the optimizer’s steps. Let’s consider the step that the optimizer takes at training iteration t . This parameter update from θ_t to θ_{t+1} happens in a one-dimensional space, defined by the update direction $\theta_{t+1} - \theta_t = s_t$. The update direction depends on the update rule of the optimizer, *e.g.* for SGD with learning rate η it is simply $s_t = -\eta g_{\mathcal{B}_t}(\theta_t)$.

We build a noise-informed univariate quadratic approximation along this update step ($\theta_t \rightarrow \theta_{t+1}$) based on the two noisy loss function observations at θ_t and θ_{t+1} and the two noisy slope observation at these two points. Examining this quadratic fit, we are able to determine where on this parabola our optimizer steps. Standardizing this, we express a step to the minimum of the loss in the update direction as $\alpha = 0$. Analogously, steps that end short of this minimum result in $\alpha < 0$, and a step over the minimum in $\alpha > 0$. These three different scenarios are illustrated in Figure 8 also showing the underlying observations that would lead to them. Figure 1 shows the distribution of α -values for two very different optimization trajectories.

Noisy observations: In order to build an approximation for the loss function in the update direction, we leverage the four observations of the function (and its derivative) that are available in each iteration. Due to the stochasticity of deep learning optimization, we also take into account the noise-level of all observations by estimating them. The first two observations are the mini-batch training losses $\mathcal{L}_{\mathcal{B}_t}(\theta_t)$, $\mathcal{L}_{\mathcal{B}_{t+1}}(\theta_{t+1})$ at point θ_t and θ_{t+1} , which are computed in every standard training loop. The mini-batch losses are averages over individual losses,

$$\begin{aligned}\mathcal{L}_{\mathcal{B}_t}(\theta_t) &= \mathbb{E}_{\mathcal{B}_t} [\ell(\theta_t)] = \frac{1}{|\mathcal{B}_t|} \sum_{n \in \mathcal{B}_t} \ell_n(\theta_t), \\ \mathcal{L}_{\mathcal{B}_{t+1}}(\theta_{t+1}) &= \mathbb{E}_{\mathcal{B}_{t+1}} [\ell(\theta_{t+1})] = \frac{1}{|\mathcal{B}_{t+1}|} \sum_{n \in \mathcal{B}_{t+1}} \ell_n(\theta_{t+1}),\end{aligned}$$

and using these individual losses, we can also compute the variances to estimate the noise-level of our loss observation,

$$\begin{aligned}\text{Var}_{\mathcal{B}_t} [\ell(\theta_t)] &= \left(\frac{1}{B_t} \sum_{n \in \mathcal{B}_t} \ell_n(\theta_t)^2 \right) - \left(\frac{1}{B_t} \sum_{n \in \mathcal{B}_t} \ell_n(\theta_t) \right)^2, \\ \text{Var}_{\mathcal{B}_{t+1}} [\ell(\theta_{t+1})] &= \left(\frac{1}{|\mathcal{B}_{t+1}|} \sum_{n \in \mathcal{B}_{t+1}} \ell_n(\theta_{t+1})^2 \right) - \left(\frac{1}{|\mathcal{B}_{t+1}|} \sum_{n \in \mathcal{B}_{t+1}} \ell_n(\theta_{t+1}) \right)^2.\end{aligned}$$

Similarly, we proceed with the slope in the update direction. To compute the slope of the loss function in the direction of the optimizer's update s_t , we project the current gradient along this update direction

$$\begin{aligned}\mathbb{E}_{\mathcal{B}_t} \left[\frac{s_t^\top \mathbf{g}(\boldsymbol{\theta}_t)}{\|s_t\|^2} \right] &= \frac{1}{|\mathcal{B}_t|} \sum_{n \in \mathcal{B}_t} \frac{s_t^\top \mathbf{g}_n(\boldsymbol{\theta}_t)}{\|s_t\|^2}, \\ \mathbb{E}_{\mathcal{B}_{t+1}} \left[\frac{s_t^\top \mathbf{g}(\boldsymbol{\theta}_{t+1})}{\|s_t\|^2} \right] &= \frac{1}{|\mathcal{B}_{t+1}|} \sum_{n \in \mathcal{B}_{t+1}} \frac{s_t^\top \mathbf{g}_n(\boldsymbol{\theta}_{t+1})}{\|s_t\|^2}.\end{aligned}$$

Just like before, we can also compute the variance of this slope, by leveraging individual gradients,

$$\begin{aligned}\text{Var}_{\mathcal{B}_t} \left[\frac{s_t^\top \mathbf{g}(\boldsymbol{\theta}_t)}{\|s_t\|^2} \right] &= \frac{1}{|\mathcal{B}_t|} \sum_{n \in \mathcal{B}_t} \left(\frac{s_t^\top \mathbf{g}_n(\boldsymbol{\theta}_t)}{\|s_t\|^2} \right)^2 - \left(\frac{1}{|\mathcal{B}_t|} \sum_{n \in \mathcal{B}_t} \frac{s_t^\top \mathbf{g}_n(\boldsymbol{\theta}_t)}{\|s_t\|^2} \right)^2, \\ \text{Var}_{\mathcal{B}_{t+1}} \left[\frac{s_t^\top \mathbf{g}(\boldsymbol{\theta}_{t+1})}{\|s_t\|^2} \right] &= \frac{1}{|\mathcal{B}_{t+1}|} \sum_{n \in \mathcal{B}_{t+1}} \left(\frac{s_t^\top \mathbf{g}_n(\boldsymbol{\theta}_{t+1})}{\|s_t\|^2} \right)^2 - \left(\frac{1}{|\mathcal{B}_{t+1}|} \sum_{n \in \mathcal{B}_{t+1}} \frac{s_t^\top \mathbf{g}_n(\boldsymbol{\theta}_{t+1})}{\|s_t\|^2} \right)^2.\end{aligned}$$

Quadratic fit & normalization: Using our (noisy) observations, we are now ready to build an approximation for the loss as a function of the step size, which we will denote as $f(\tau)$. We assume a quadratic function for f , which follows recent reports for the loss landscape of neural networks [43], *i.e.* a function $f(\tau) = w_0 + w_1\tau + w_2\tau^2$ parameterized by $\mathbf{w} \in \mathbb{R}^3$. We further assume a Gaussian likelihood of the form

$$p(\tilde{\mathbf{f}} | \mathbf{w}, \Phi) = \mathcal{N}(\tilde{\mathbf{f}}; \Phi^\top \mathbf{w}, \Lambda) \quad (9)$$

for observations $\tilde{\mathbf{f}}$ of the loss and its slope. The observation matrix Φ and the noise matrix of the observations Λ are

$$\Phi = \begin{pmatrix} 1 & 1 & 0 & 0 \\ \tau_1 & \tau_2 & 1 & 1 \\ \tau_1^2 & \tau_2^2 & 2\tau_1 & 2\tau_2 \end{pmatrix}, \quad \Lambda = \begin{pmatrix} \sigma_{\tilde{f}_1} & 0 & 0 & 0 \\ 0 & \sigma_{\tilde{f}_2} & 0 & 0 \\ 0 & 0 & \sigma_{\tilde{f}'_1} & 0 \\ 0 & 0 & 0 & \sigma_{\tilde{f}'_2} \end{pmatrix},$$

where τ denotes the position and σ denotes the noise-level estimate of the observation. The maximum likelihood solution of Equation (9) for the parameters of our quadratic fit is given by

$$\mathbf{w} = (\Phi \Lambda^{-1} \Phi^\top) \Phi \Lambda^{-1} \tilde{\mathbf{f}}. \quad (10)$$

Once we have the quadratic fit of the univariate loss function in the update direction, we normalize the scales such that the resulting α -value expresses the effective step taken by the optimizer sketched in Figure 8.

The α -quantity is related to recent line search approaches [26, 40]. However, instead of searching for an acceptable step by repeated attempts, we instead report the effect of the current step size selection. This information could indeed be used to automatically adapt the learning rate during the training process. But, as discussed in Section 3.3, it isn't trivial what the "correct" decision is, as it might depend on the optimization problem, the training phase, and other factors.

B.3. CABS criterion: Coupling adaptive batch sizes with learning rates (CABS)

The CABS criterion, proposed in [4], can be used to adapt the mini-batch size during training with SGD. It relies on the gradient noise and approximately optimizes the objective's expected gain per cost. The adaptation rule is (with learning rate η)

$$|\mathcal{B}| \leftarrow \eta \frac{\text{Tr}(\Sigma_P(\boldsymbol{\theta}))}{\mathcal{L}_P(\boldsymbol{\theta})}, \quad (11)$$

and the practical implementation approximates $\mathcal{L}_P(\boldsymbol{\theta}) \approx \mathcal{L}_{\mathcal{B}}(\boldsymbol{\theta})$, $\text{Tr}(\Sigma_P(\boldsymbol{\theta})) \approx \frac{|\mathcal{B}|-1}{|\mathcal{B}|} \text{Tr}(\hat{\Sigma}_{\mathcal{B}}(\boldsymbol{\theta}))$ (compare equations (10, 22) and first paragraph of Section 4 in [4]). This yields the quantity computed in cockpit's CABS instrument,

$$|\mathcal{B}| \leftarrow \eta \frac{\frac{1}{|\mathcal{B}|} \sum_{j=1}^D \sum_{n \in \mathcal{B}} [\mathbf{g}_n(\boldsymbol{\theta}) - \mathbf{g}_{\mathcal{B}}(\boldsymbol{\theta})]_j^2}{\mathcal{L}_{\mathcal{B}}(\boldsymbol{\theta})}. \quad (12)$$

B.4. Early-stopping criterion for SGD (EarlyStopping)

The empirical risk $\mathcal{L}_{\mathcal{D}}(\boldsymbol{\theta})$, and the mini-batch loss $\mathcal{L}_{\mathcal{B}}(\boldsymbol{\theta})$ are only estimators of the target objective $\mathcal{L}_P(\boldsymbol{\theta})$. [25] motivate $p(\mathbf{g}_{\mathcal{B}, \mathcal{D}}(\boldsymbol{\theta}) \mid \mathbf{g}_P(\boldsymbol{\theta}) = \mathbf{0})$ as a measure for detecting noise in the finite data sets \mathcal{B}, \mathcal{D} due to sampling from P . They propose an evidence-based (EB) criterion for early stopping the training procedure based on mini-batch statistics, and model $p(\mathbf{g}_{\mathcal{B}}(\boldsymbol{\theta}))$ with a sampled diagonal variance approximation (compare Equation (8)),

$$p(\mathbf{g}_{\mathcal{B}}(\boldsymbol{\theta})) \approx \prod_{j=1}^D \mathcal{N} \left([\mathbf{g}_P(\boldsymbol{\theta})]_j; \frac{[\hat{\Sigma}_{\mathcal{B}}(\boldsymbol{\theta})]_{j,j}}{|\mathcal{B}|} \right). \quad (13)$$

Their SGD stopping criterion is

$$\frac{2}{D} [\log p(\mathbf{g}_{\mathcal{B}}(\boldsymbol{\theta})) - \mathbb{E}_{\mathbf{g}_{\mathcal{B}}(\boldsymbol{\theta}) \sim p(\mathbf{g}_{\mathcal{B}}(\boldsymbol{\theta}))} [\log p(\mathbf{g}_{\mathcal{B}}(\boldsymbol{\theta}))]] > 0, \quad (14a)$$

and translates into

$$1 - \frac{|\mathcal{B}|}{D} \sum_{j=1}^D \frac{[\mathbf{g}_{\mathcal{B}}(\boldsymbol{\theta})]_j^2}{[\hat{\Sigma}_{\mathcal{B}}(\boldsymbol{\theta})]_{j,j}} > 0, \quad (14b)$$

$$1 - \frac{|\mathcal{B}|}{D} \sum_{d=1}^D \frac{[\mathbf{g}_{\mathcal{B}}(\boldsymbol{\theta})]_d^2}{\frac{1}{|\mathcal{B}| - 1} \sum_{n \in \mathcal{B}} [\mathbf{g}_n(\boldsymbol{\theta}) - \mathbf{g}_{\mathcal{B}}(\boldsymbol{\theta})]_d^2} > 0, \quad (14c)$$

$$1 - \frac{|\mathcal{B}|(|\mathcal{B}| - 1)}{D} \sum_{d=1}^D \frac{[\mathbf{g}_{\mathcal{B}}(\boldsymbol{\theta})]_d^2}{\left(\sum_{n \in \mathcal{B}} [\mathbf{g}_n(\boldsymbol{\theta})]_d^2 \right) - |\mathcal{B}| [\mathbf{g}_{\mathcal{B}}(\boldsymbol{\theta})]_d^2} > 0. \quad (14d)$$

COCKPIT's EarlyStopping quantity computes the left-hand side of Equation (14d).

B.5. Individual gradient element histograms (GradHist1d, GradHist2d)

For the $|\mathcal{B}| \times D$ individual gradient elements, COCKPIT's GradHist1d instrument displays a histogram of

$$\{\mathbf{g}_n(\boldsymbol{\theta}_j)\}_{n \in \mathcal{B}, j=1, \dots, D}. \quad (15)$$

COCKPIT's GradHist2d instrument displays a two-dimensional histogram of the $|\mathcal{B}| \times D$ tuples

$$\{(\boldsymbol{\theta}_j, \mathbf{g}_n(\boldsymbol{\theta}_j))\}_{n \in \mathcal{B}, j=1, \dots, D} \quad (16)$$

and the marginalized one-dimensional histograms over the parameter- and gradient axes.

B.6. Gradient tests (NormTest, InnerTest, OrthoTest)

[6, 8] propose batch size adaptation schemes based on the gradient noise. They formulate geometric constraints between population and mini-batch gradient and accessible approximations that can be probed to decide whether the mini-batch size should be increased. Because mini-batches are i.i.d. from P , it holds that

$$\mathbb{E} [\mathbf{g}_{\mathcal{B}}(\boldsymbol{\theta})] = \mathbf{g}_P(\boldsymbol{\theta}), \quad (17a)$$

$$\mathbb{E} [\mathbf{g}_{\mathcal{B}}(\boldsymbol{\theta})^\top \mathbf{g}_P(\boldsymbol{\theta})] = \|\mathbf{g}_P(\boldsymbol{\theta})\|^2. \quad (17b)$$

The above works propose enforcing other weaker similarity in expectation during optimization. These geometric constraints reduce to basic vector geometry (see Figure 9 (a) for an overview of the relevant vectors). We recall their formulation here for consistency and derive the practical versions, which can be computed from training observables and are used in COCKPIT (consult Figure 9 (b) for the visualization).

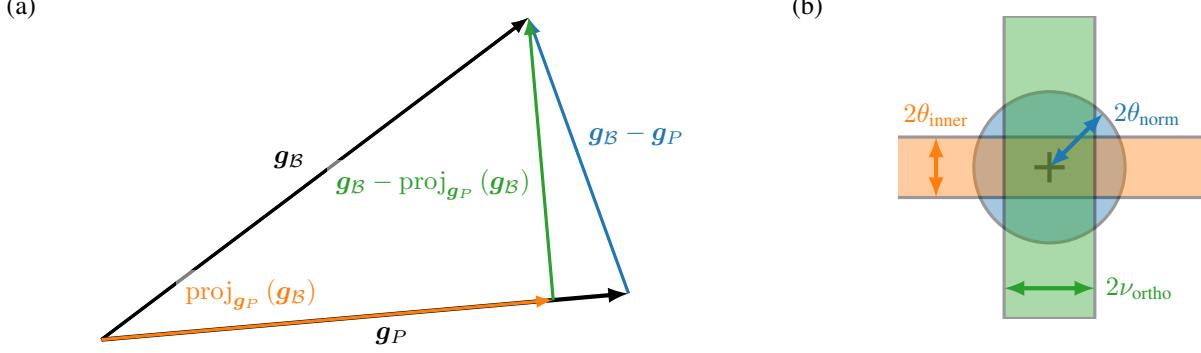


Figure 9. **Conceptual sketch for gradient tests.** (a) Relevant vectors to formulate the geometric constraints between population and mini-batch gradient probed by the gradient tests. (b) Gradient test visualization in COCKPIT.

B.6.1 Norm test (NormTest)

The norm test [8] constrains the residual norm $\|\mathbf{g}_B(\theta) - \mathbf{g}_P(\theta)\|$, rescaled by $\|\mathbf{g}_P(\theta)\|$. This gives rise to a standardized ball of radius $\theta_{\text{norm}} \in (0, \infty)$ around the population gradient, where the mini-batch gradient should reside. [6] set $\theta_{\text{norm}} = 0.9$ in their experiments and increase the batch size if (in the practical version, see below) the following constraint is not fulfilled

$$\mathbb{E} \left[\frac{\|\mathbf{g}_B(\theta) - \mathbf{g}_P(\theta)\|^2}{\|\mathbf{g}_P(\theta)\|^2} \right] \leq \theta_{\text{norm}}^2. \quad (18a)$$

Instead of taking the expectation over mini-batches, [8] note that the above will be satisfied if

$$\frac{1}{|\mathcal{B}|} \mathbb{E} \left[\frac{\|\mathbf{g}_n(\theta) - \mathbf{g}_P(\theta)\|^2}{\|\mathbf{g}_P(\theta)\|^2} \right] \leq \theta_{\text{norm}}^2. \quad (18b)$$

They propose a practical form of this test,

$$\frac{1}{|\mathcal{B}|(|\mathcal{B}| - 1)} \frac{\sum_{n \in \mathcal{B}} \|\mathbf{g}_n(\theta) - \mathbf{g}_B(\theta)\|^2}{\|\mathbf{g}_B(\theta)\|^2} \leq \theta_{\text{norm}}^2, \quad (19a)$$

which can be computed from mini-batch statistics. Rearranging

$$\sum_{n \in \mathcal{B}} \|\mathbf{g}_n(\theta) - \mathbf{g}_B(\theta)\|^2 = \left(\sum_{n \in \mathcal{B}} \|\mathbf{g}_n(\theta)\|^2 \right) - |\mathcal{B}| \|\mathbf{g}_B(\theta)\|^2, \quad (19b)$$

we arrive at

$$\frac{1}{|\mathcal{B}|(|\mathcal{B}| - 1)} \left[\frac{\sum_{n \in \mathcal{B}} \|\mathbf{g}_n(\theta)\|^2}{\|\mathbf{g}_B(\theta)\|^2} - |\mathcal{B}| \right] \leq \theta_{\text{norm}}^2 \quad (19c)$$

that leverages the norm of both the mini-batch and the individual gradients, which can be aggregated over parameters during a backward pass. COCKPIT’s NormTest corresponds to the maximum radius θ_{norm} for which the above inequality holds.

B.6.2 Inner product test (InnerTest)

The inner product test [6] constrains the projection of $\mathbf{g}_B(\theta)$ onto $\mathbf{g}_P(\theta)$ (compare Figure 9 (a)),

$$\text{proj}_{\mathbf{g}_P(\theta)}(\mathbf{g}_B(\theta)) = \frac{\mathbf{g}_B(\theta)^\top \mathbf{g}_P(\theta)}{\|\mathbf{g}_P(\theta)\|^2} \mathbf{g}_P(\theta), \quad (20)$$

rescaled by $\|\mathbf{g}_P(\boldsymbol{\theta})\|$. This restricts the mini-batch gradient to reside in a standardized band of relative width $\theta_{\text{inner}} \in (0, \infty)$ around the population risk gradient. [6] use $\theta_{\text{inner}} = 0.9$ (in the practical version, see below) to adapt the batch size if the parallel component's variance does not satisfy the condition

$$\text{Var} \left(\frac{\mathbf{g}_B(\boldsymbol{\theta})^\top \mathbf{g}_P(\boldsymbol{\theta})}{\|\mathbf{g}_P(\boldsymbol{\theta})\|^2} \right) = \mathbb{E} \left[\left(\frac{\mathbf{g}_B(\boldsymbol{\theta})^\top \mathbf{g}_P(\boldsymbol{\theta})}{\|\mathbf{g}_P(\boldsymbol{\theta})\|^2} - 1 \right)^2 \right] \leq \theta_{\text{inner}}^2 \quad (21a)$$

(note that by Equation (17) we have $\mathbb{E} \left[\frac{\mathbf{g}_B(\boldsymbol{\theta})^\top \mathbf{g}_P(\boldsymbol{\theta})}{\|\mathbf{g}_P(\boldsymbol{\theta})\|^2} \right] = 1$). [6] bounds Equation (21a) by the individual gradient variance,

$$\frac{1}{|\mathcal{B}|} \text{Var} \left(\frac{\mathbf{g}_n(\boldsymbol{\theta})^\top \mathbf{g}_P(\boldsymbol{\theta})}{\|\mathbf{g}_P(\boldsymbol{\theta})\|^2} \right) = \frac{1}{|\mathcal{B}|} \mathbb{E} \left[\left(\frac{\mathbf{g}_n(\boldsymbol{\theta})^\top \mathbf{g}_P(\boldsymbol{\theta})}{\|\mathbf{g}_P(\boldsymbol{\theta})\|^2} - 1 \right)^2 \right] \leq \theta_{\text{inner}}^2. \quad (21b)$$

They then propose a practical form of Equation (21b), which uses the mini-batch sample variance,

$$\frac{1}{|\mathcal{B}|} \text{Var} \left(\frac{\mathbf{g}_n(\boldsymbol{\theta})^\top \mathbf{g}_B(\boldsymbol{\theta})}{\|\mathbf{g}_B(\boldsymbol{\theta})\|^2} \right) = \frac{1}{|\mathcal{B}|(|\mathcal{B}| - 1)} \left[\sum_{n \in \mathcal{B}} \left(\frac{\mathbf{g}_n(\boldsymbol{\theta})^\top \mathbf{g}_B(\boldsymbol{\theta})}{\|\mathbf{g}_B(\boldsymbol{\theta})\|^2} - 1 \right)^2 \right] \leq \theta_{\text{inner}}^2. \quad (22a)$$

Expanding

$$\sum_{n \in \mathcal{B}} \left(\frac{\mathbf{g}_n(\boldsymbol{\theta})^\top \mathbf{g}_B(\boldsymbol{\theta})}{\|\mathbf{g}_B(\boldsymbol{\theta})\|^2} - 1 \right)^2 = \frac{\sum_{n \in \mathcal{B}} (\mathbf{g}_n(\boldsymbol{\theta})^\top \mathbf{g}_B(\boldsymbol{\theta}))^2}{\|\mathbf{g}_B(\boldsymbol{\theta})\|^4} - |\mathcal{B}| \quad (22b)$$

and inserting Equation (22b) into Equation (22a) yields

$$\frac{1}{|\mathcal{B}|(|\mathcal{B}| - 1)} \left[\frac{\sum_{n \in \mathcal{B}} (\mathbf{g}_n(\boldsymbol{\theta})^\top \mathbf{g}_B(\boldsymbol{\theta}))^2}{\|\mathbf{g}_B(\boldsymbol{\theta})\|^4} - |\mathcal{B}| \right] \leq \theta_{\text{inner}}^2. \quad (22c)$$

It relies on pairwise scalar products between individual gradients, which can be aggregated over layers during backpropagation. COCKPIT's `InnerTest` quantity computes the maximum band width θ_{inner} that satisfies Equation (22c).

B.6.3 Orthogonality test (`OrthoTest`)

In contrast to the inner product test (Appendix B.6.2) which constrains the projection (Equation (20)), the orthogonality test [6] constrains the orthogonal part (see Figure 9 (a))

$$\mathbf{g}_B(\boldsymbol{\theta}) - \text{proj}_{\mathbf{g}_P(\boldsymbol{\theta})}(\mathbf{g}_B(\boldsymbol{\theta})), \quad (23)$$

rescaled by $\|\mathbf{g}_P(\boldsymbol{\theta})\|$. This restricts the mini-batch gradient to a standardized band of relative width $\nu_{\text{ortho}} \in (0, \infty)$ parallel to the population gradient. [6] uses $\nu = \tan(80^\circ) \approx 5.84$ (in the practical version, see below) to adapt the batch size if the following condition is violated,

$$\mathbb{E} \left[\left\| \frac{\mathbf{g}_B(\boldsymbol{\theta}) - \text{proj}_{\mathbf{g}_P(\boldsymbol{\theta})}(\mathbf{g}_B(\boldsymbol{\theta}))}{\|\mathbf{g}_P(\boldsymbol{\theta})\|} \right\|^2 \right] \leq \nu_{\text{ortho}}^2. \quad (24a)$$

Expanding the norm, and inserting Equation (20), this simplifies to

$$\begin{aligned} \mathbb{E} \left[\left\| \frac{\mathbf{g}_B(\boldsymbol{\theta})}{\|\mathbf{g}_P(\boldsymbol{\theta})\|} - \frac{\mathbf{g}_B(\boldsymbol{\theta})^\top \mathbf{g}_P(\boldsymbol{\theta})}{\|\mathbf{g}_P(\boldsymbol{\theta})\|^2} \frac{\mathbf{g}_P(\boldsymbol{\theta})}{\|\mathbf{g}_P(\boldsymbol{\theta})\|} \right\|^2 \right] &\leq \nu_{\text{ortho}}^2, \\ \mathbb{E} \left[\frac{\|\mathbf{g}_B(\boldsymbol{\theta})\|^2}{\|\mathbf{g}_P(\boldsymbol{\theta})\|^2} - \frac{(\mathbf{g}_B(\boldsymbol{\theta})^\top \mathbf{g}_P(\boldsymbol{\theta}))^2}{\|\mathbf{g}_P(\boldsymbol{\theta})\|^4} \right] &\leq \nu_{\text{ortho}}^2. \end{aligned} \quad (24b)$$

[6] bound this inequality using individual gradients instead,

$$\frac{1}{|\mathcal{B}|} \mathbb{E} \left[\left\| \frac{\mathbf{g}_n(\boldsymbol{\theta})}{\|\mathbf{g}_P(\boldsymbol{\theta})\|^2} - \frac{\mathbf{g}_n(\boldsymbol{\theta})^\top \mathbf{g}_P(\boldsymbol{\theta})}{\|\mathbf{g}_P(\boldsymbol{\theta})\|^2} \frac{\mathbf{g}_P(\boldsymbol{\theta})}{\|\mathbf{g}_P(\boldsymbol{\theta})\|} \right\|^2 \right] \leq \nu_{\text{ortho}}^2. \quad (24\text{c})$$

They propose the practical form

$$\frac{1}{|\mathcal{B}|(|\mathcal{B}| - 1)} \mathbb{E} \left[\left\| \frac{\mathbf{g}_n(\boldsymbol{\theta})}{\|\mathbf{g}_{\mathcal{B}}(\boldsymbol{\theta})\|} - \frac{\mathbf{g}_n(\boldsymbol{\theta})^\top \mathbf{g}_{\mathcal{B}}(\boldsymbol{\theta})}{\|\mathbf{g}_{\mathcal{B}}(\boldsymbol{\theta})\|^2} \frac{\mathbf{g}_{\mathcal{B}}(\boldsymbol{\theta})}{\|\mathbf{g}_{\mathcal{B}}(\boldsymbol{\theta})\|} \right\|^2 \right] \leq \nu_{\text{ortho}}^2, \quad (25\text{a})$$

which simplifies to

$$\frac{1}{|\mathcal{B}|(|\mathcal{B}| - 1)} \sum_{n \in \mathcal{B}} \left(\frac{\|\mathbf{g}_n(\boldsymbol{\theta})\|^2}{\|\mathbf{g}_{\mathcal{B}}(\boldsymbol{\theta})\|^2} - 2 \frac{(\mathbf{g}_n(\boldsymbol{\theta})^\top \mathbf{g}_{\mathcal{B}}(\boldsymbol{\theta}))^2}{\|\mathbf{g}_{\mathcal{B}}(\boldsymbol{\theta})\|^4} + 1 \right) \leq \nu_{\text{ortho}}^2. \quad (25\text{b})$$

It relies on pairwise scalar products between individual gradients which can be aggregated over layers during a backward pass. COCKPIT’s OrthTest quantity computes the maximum band width ν_{ortho} which satisfies Equation (25b).

Relation to acute angle test: Recently, a novel “acute angle test” was proposed by [3]. While the theoretical constraint between $\mathbf{g}_{\mathcal{B}}(\boldsymbol{\theta})$ and $\mathbf{g}_P(\boldsymbol{\theta})$ differs from the orthogonality test, the practical versions coincide. Hence, we do not incorporate the acute angle here.

B.7. Hessian maximum eigenvalue (HessMaxEV)

The Hessian’s maximum eigenvalue $\lambda_{\max}(\mathbf{H}_{\mathcal{B}}(\boldsymbol{\theta}))$ is computed with an iterative eigensolver from Hessian-vector products through PYTORCH’s automatic differentiation [30]. Like [44], we employ power iterations with similar **default stopping parameters** (stop after at most 100 iterations, or if the iterate does converged with a relative and absolute tolerance of $10^{-3}, 10^{-6}$, respectively) to compute $\lambda_{\max}(\mathbf{H}_{\mathcal{B}}(\boldsymbol{\theta}))$ through the HessMaxEV quantity in COCKPIT.

In principle, more sophisticated eigensolvers (for example Arnoldi’s method) could be applied to converge in fewer iterations or compute eigenvalues other than the leading ones. [41] empirically demonstrate that the FLOP ratio between power iteration and implicitly restarted Arnoldi method can reach values larger than 100. While we can use such a beneficial method on a CPU through `scipy.sparse.linalg.eigsh` we are restricted to the GPU-compatible power iteration for GPU training. We expect that extending the support of popular machine learning libraries like PYTORCH for such iterative eigensolvers on GPUs can help to save computation time.

$$\lambda_{\max}(\mathbf{H}_{\mathcal{B}}(\boldsymbol{\theta})) = \max_{\|\mathbf{v}\|=1} \|\mathbf{H}_{\mathcal{B}}(\boldsymbol{\theta})\mathbf{v}\| = \max_{\mathbf{v} \in \mathbb{R}^D} \frac{\mathbf{v}^\top \mathbf{H}_{\mathcal{B}}(\boldsymbol{\theta})\mathbf{v}}{\mathbf{v}^\top \mathbf{v}}. \quad (26)$$

B.8. Hessian trace (HessTrace)

In comparison to [44], who leverage Hessian-vector products [30] to estimate the Hessian trace, we compute the exact value $\text{Tr}(\mathbf{H}_{\mathcal{B}}(\boldsymbol{\theta}))$ with the HessTrace quantity in COCKPIT by aggregating the output of BACKPACK’s **DiagHessian** extension, which computes the diagonal entries of $\mathbf{H}_{\mathcal{B}}(\boldsymbol{\theta})$. Alternatively, the trace can also be estimated from the generalized Gauss-Newton matrix, or an MC-sampled approximation thereof.

B.9. Takeuchi Information Criterion (TIC) (TICDiag, TICTrace)

Recent work by [38] suggests that optimizer convergence speed and generalization is mainly influenced by curvature and gradient noise; and hence their interaction is crucial to understanding the generalization and optimization behavior of deep neural networks. They reinvestigate the Takeuchi Information criterion [37], an estimator for the generalization gap in overparameterized maximum likelihood estimation. At a local minimum $\boldsymbol{\theta}^*$, the generalization gap is estimated by the TIC

$$\frac{1}{|\mathcal{D}|} \text{Tr} (\mathbf{H}_P(\boldsymbol{\theta}^*)^{-1} \mathbf{C}_P(\boldsymbol{\theta}^*)), \quad (27)$$

where $\mathbf{H}_P(\boldsymbol{\theta}^*)$ is the population Hessian and $\mathbf{C}_P(\boldsymbol{\theta}^*)$ is the gradient’s uncentered second moment at the local minimum,

$$\mathbf{C}_P(\boldsymbol{\theta}^*) = \int \nabla_{\boldsymbol{\theta}} \ell(f(\boldsymbol{\theta}^*, \mathbf{x}), \mathbf{y}) (\nabla_{\boldsymbol{\theta}} \ell(f(\boldsymbol{\theta}^*, \mathbf{x}), \mathbf{y}))^\top P(\mathbf{x}, \mathbf{y}) d\mathbf{x} d\mathbf{y}.$$

Both matrices are inaccessible in practice. In their experiments, [38] propose the approximation $\text{Tr}(\mathbf{C})/\text{Tr}(\mathbf{H})$ for $\text{Tr}(\mathbf{H}^{-1}\mathbf{C})$. They also replace the Hessian by the Fisher as it is easier to compute. With these practical simplifications, they investigate the TIC of trained neural networks where the curvature and noise matrix are evaluated on a large data set.

The TIC provided in COCKPIT differs from this setting, since by design we want to observe quantities during training, while avoiding additional model predictions. Also, BACKPACK provides access to the Hessian; hence we don't need to use the Fisher. We propose the following two approximations of the TIC from a mini-batch:

- **TICTrace**: Uses the approximation of [38] which replaces the matrix-product trace by the product of traces,

$$\frac{\text{Tr}(\mathbf{C}_{\mathcal{B}}(\boldsymbol{\theta}))}{\text{Tr}(\mathbf{H}_{\mathcal{B}}(\boldsymbol{\theta}))} = \frac{\frac{1}{|\mathcal{B}|} \sum_{n \in \mathcal{B}} \|\mathbf{g}_n(\boldsymbol{\theta})\|^2}{\text{Tr}(\mathbf{H}_{\mathcal{B}}(\boldsymbol{\theta}))}. \quad (28)$$

- **TICDiag**: Uses a diagonal approximation of the Hessian, which is cheap to invert,

$$\text{Tr}(\text{diag}(\mathbf{H}_{\mathcal{B}}(\boldsymbol{\theta}))^{-1} \mathbf{C}_{\mathcal{B}}(\boldsymbol{\theta})) = \frac{1}{|\mathcal{B}|} \sum_{j=1}^D [\mathbf{H}_{\mathcal{B}}(\boldsymbol{\theta})]_{j,j}^{-1} \left[\sum_{n \in \mathcal{B}} \mathbf{g}_n(\boldsymbol{\theta})^{\odot 2} \right]_j. \quad (29)$$

B.10. Gradient signal-to-noise-ratio (MeanGSNR)

The gradient signal-to-noise-ratio $\text{GSNR}([\boldsymbol{\theta}]_j) \in \mathbb{R}$ for a single parameter $[\boldsymbol{\theta}]_j$ is defined as

$$\text{GSNR}([\boldsymbol{\theta}]_j) = \frac{\mathbb{E}_{(\mathbf{x}, \mathbf{y}) \sim P} \left[[\nabla_{\boldsymbol{\theta}} \ell(f(\boldsymbol{\theta}, \mathbf{x}), \mathbf{y})]_j \right]^2}{\text{Var}_{(\mathbf{x}, \mathbf{y}) \sim P} \left[[\nabla_{\boldsymbol{\theta}} \ell(f(\boldsymbol{\theta}, \mathbf{x}), \mathbf{y})]_j \right]} = \frac{[\mathbf{g}_P(\boldsymbol{\theta})]_j^2}{[\boldsymbol{\Sigma}_P(\boldsymbol{\theta})]_{j,j}}. \quad (30)$$

[24] uses it to explain generalization properties of models in the early training phase. We apply their estimation to mini-batches,

$$\text{GSNR}([\boldsymbol{\theta}]_j) \approx \frac{[\mathbf{g}_{\mathcal{B}}(\boldsymbol{\theta})]_j^2}{\frac{|\mathcal{B}| - 1}{|\mathcal{B}|} \left[\hat{\boldsymbol{\Sigma}}_{\mathcal{B}}(\boldsymbol{\theta}) \right]_{j,j}} = \frac{[\mathbf{g}_{\mathcal{B}}(\boldsymbol{\theta})]_j^2}{\left(\sum_{n \in \mathcal{B}} [\mathbf{g}_n(\boldsymbol{\theta})]_j^2 \right) - |\mathcal{B}| [\mathbf{g}_{\mathcal{B}}(\boldsymbol{\theta})]_j^2}. \quad (31a)$$

Inspired by [24], COCKPIT's MeanGSNR computes the average GSNR over all parameters,

$$\frac{1}{D} \sum_{j=1}^D \text{GSNR}([\boldsymbol{\theta}]_j). \quad (31b)$$

C. Implementation details and additional benchmarks

In this section, we provide more details about our implementation (Appendix C.1) to access the desired quantities with as little overhead as possible. Additionally, we present more benchmarks for individual instruments (Appendix C.2.1) and COCKPIT configurations (Appendix C.2.2). These are similar but extended versions of the ones presented in Figures 6 and 7 in the main text. Lastly, we benchmark different implementations of computing the two-dimensional gradient histogram (Appendix C.3), identifying a computational bottleneck for its current GPU implementation.

Hardware details: Throughout this Further, we are grateful to Agustinus Kristiadi, Alexandra Gessner, Christian Fröhlich, Filip de Roos, Jonathan Wenger, Julia Grosse, Lukas Tatzel, Marius Hobbahn, and Nicholas Krämer for providing feedback to the manuscript. we conducted benchmarks on the following setup

- **CPU:** Intel Core i7-8700K CPU @ 3.70 GHz × 12 (32 GB)
- **GPU:** NVIDIA GeForce RTX 2080 Ti (11 GB)

C.1. Hooks & Memory benchmarks

To improve memory consumption, we compact information during the backward pass by adding hooks to the neural network’s layers. These are executed after BACKPACK extensions and have access to the quantities computed therein. They compress information to what is requested by a quantity and free the memory occupied by BACKPACK buffers. Such savings primarily depend on the parameter distribution over layers, and are bigger for more balanced architectures (compare Figure 10).

Example: Say, we want to compute a histogram over the $|\mathcal{B}| \times D$ individual gradient elements of a network. Suppose that $|\mathcal{B}| = 128$ and the model is DEEPOBS’s CIFAR-10 3C3D test problem with 895,210 parameters. Given that every parameter is stored in single precision, the model requires $895,210 \times 4$ Bytes ≈ 3.41 MB. Storing the individual gradients will require $128 \times 895,210 \times 4$ Bytes ≈ 437 MB (for larger networks this quickly exceeds the available memory as the individual gradients occupy $|\mathcal{B}|$ times the model size). If instead, the layer-wise individual gradients are condensed into histograms of negligible size and immediately freed afterwards during backpropagation, the maximum memory overhead reduces to storing the individual gradients of the largest layer. For our example, the largest layer has 589,824 parameters, and the associated individual gradients will require $128 \times 589,824 \times 4$ Bytes ≈ 288 MB, saving roughly 149 MB of RAM. In practice, we observe slightly larger savings, see Figure 10 (c).

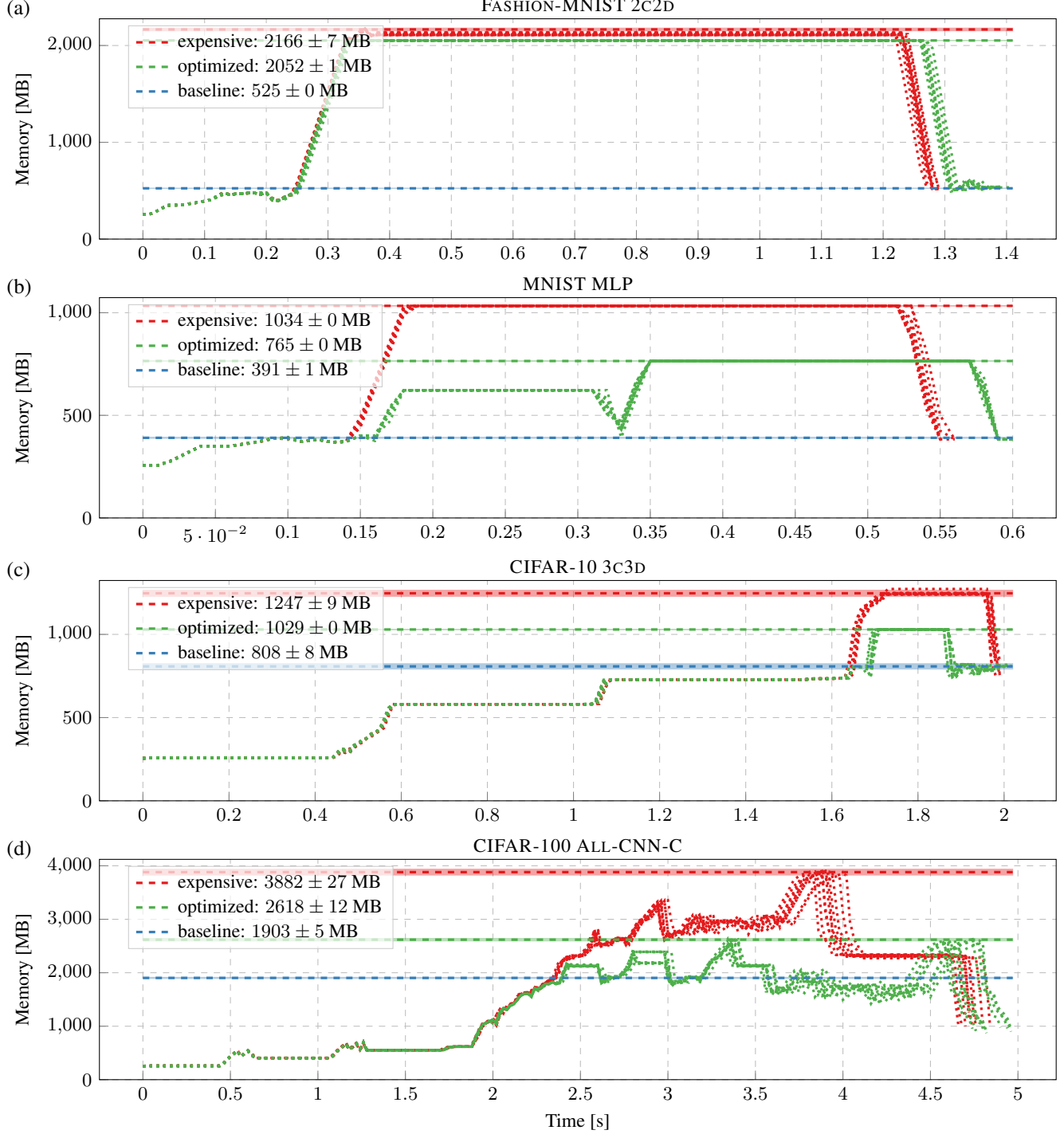


Figure 10. **Memory consumption and savings with hooks** during one forward-backward step on a CPU for different DEEPOBS problems. We compare three settings; i) without COCKPIT (baseline); ii) COCKPIT with `GradHist1d` with BACKPACK (expensive); iii) COCKPIT with `GradHist1d` with BACKPACK and additional hooks (optimized). Peak memory consumptions are highlighted by horizontal dashed bars and shown in the legend. Shaded areas, if visible, fill two standard deviations above and below the mean value, all of them result from ten independent runs. Dotted lines indicate individual runs. Our optimized approach allows to free obsolete tensors during backpropagation and thereby reduces memory consumption. From top to bottom: the effect is less pronounced for architectures that concentrate the majority of parameters in a single layer ((a) 3, 274, 634 total, 3, 211, 264 largest layer) and increases for more balanced networks (b) 1, 336, 610 total, 784, 000 largest layer, (c): 895, 210 total, 589, 824 largest layer).

C.2. Additional run time benchmarks

C.2.1 Individual instrument overhead

To estimate the computational overhead for individual instruments, we run COCKPIT with that instrument for 32 iterations, tracking at every step. Training proceeds with the default batch size specified by the DEEPOBS problem and uses SGD with learning rate 10^{-3} . We measure the time between iterations 1 and 32, and average for the overhead per step. Every such estimate is repeated over 10 random seeds to obtain mean and error bars as reported in Figure 6.

Note that this protocol does *not* include initial overhead for setting up data loading and also does *not* include the time for evaluating train/test loss on a larger data set, which is usually done by practitioners. Hence, we even expect the shown overheads to be smaller in a conventional training loop which includes the above steps.

Individual overhead on GPU versus CPU: Figure 11 and Figure 12 show the individual overhead for four different DEEPOBS problems on GPU and CPU, respectively. The left part of Figure 11 (c) corresponds to Figure 6. Right panels show the expensive quantities, which we omitted in the main text as they were expected to be expensive due to their computational work (HessMaxEV) or bottlenecks in the implementation (GradHist2d, see Appendix C.3 for details). We see that they are in many cases equally or more expensive than computing all other instruments. Another expected feature of the GPU-to-CPU comparison is that parallelism on the CPU is significantly less pronounced. Hence, we observe an increased overhead for all quantities that contain non-linear transformations and contractions of the high-dimensional individual gradients, or require additional backpropagations (curvature).

C.2.2 Configuration overhead

For the estimation of different COCKPIT configuration overheads, we use almost the same setting as described above, training for 512 iterations and tracking only every specified interval.

Configuration overhead on GPU versus CPU: Figure 13 and Figure 14 show the configuration overhead for four different DEEPOBS problems. The bottom left part of Figure 13 corresponds to Figure 7. In general, we observe that increased parallelism can be exploited on a GPU, leading to smaller overheads in comparison to a CPU.

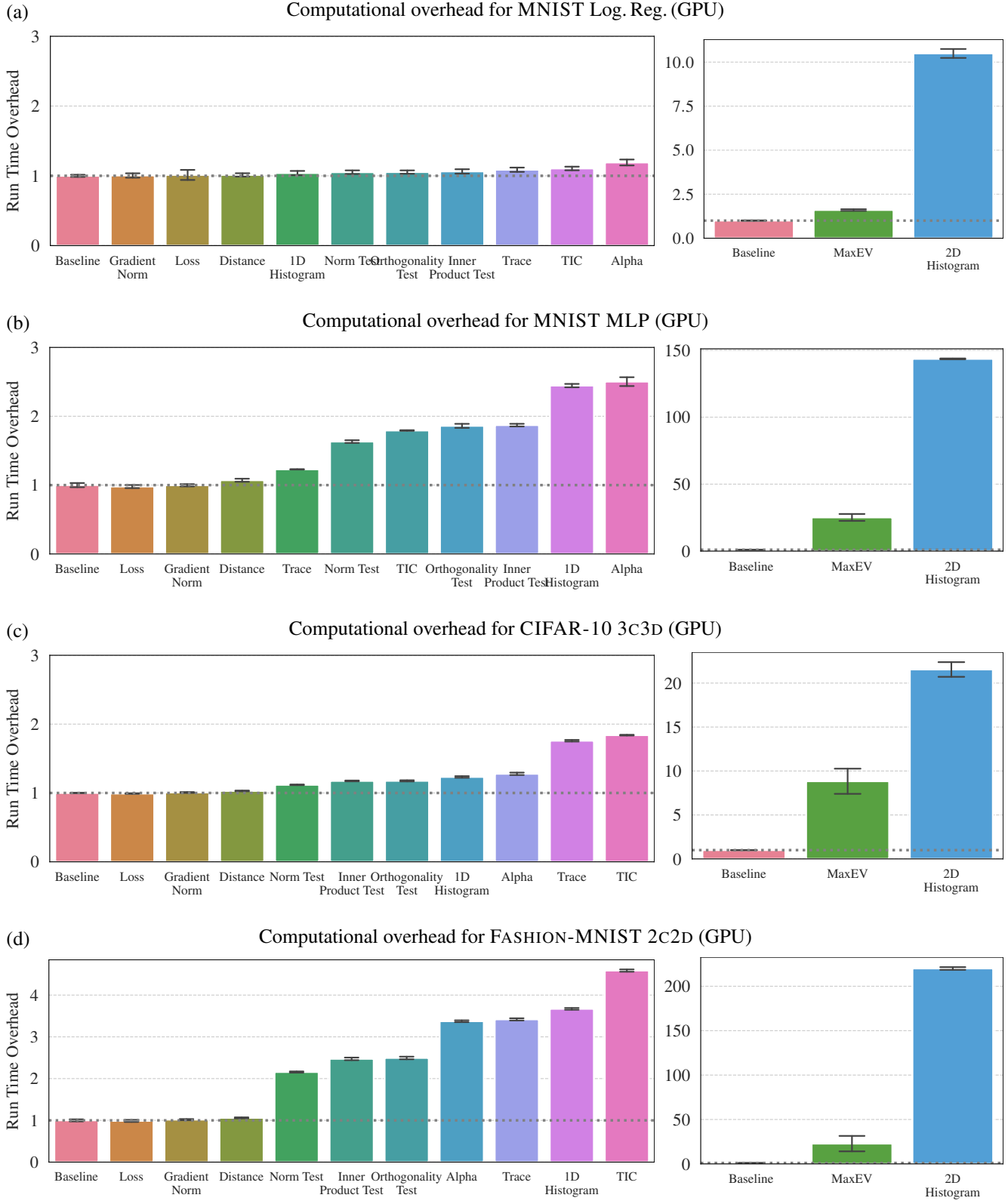


Figure 11. Individual overhead of COCKPIT’s instruments on GPU for four different problems. All run times are shown as multiples of the *baseline* without tracking. Expensive quantities are displayed in separate panels on the right. Experimental details in the text.

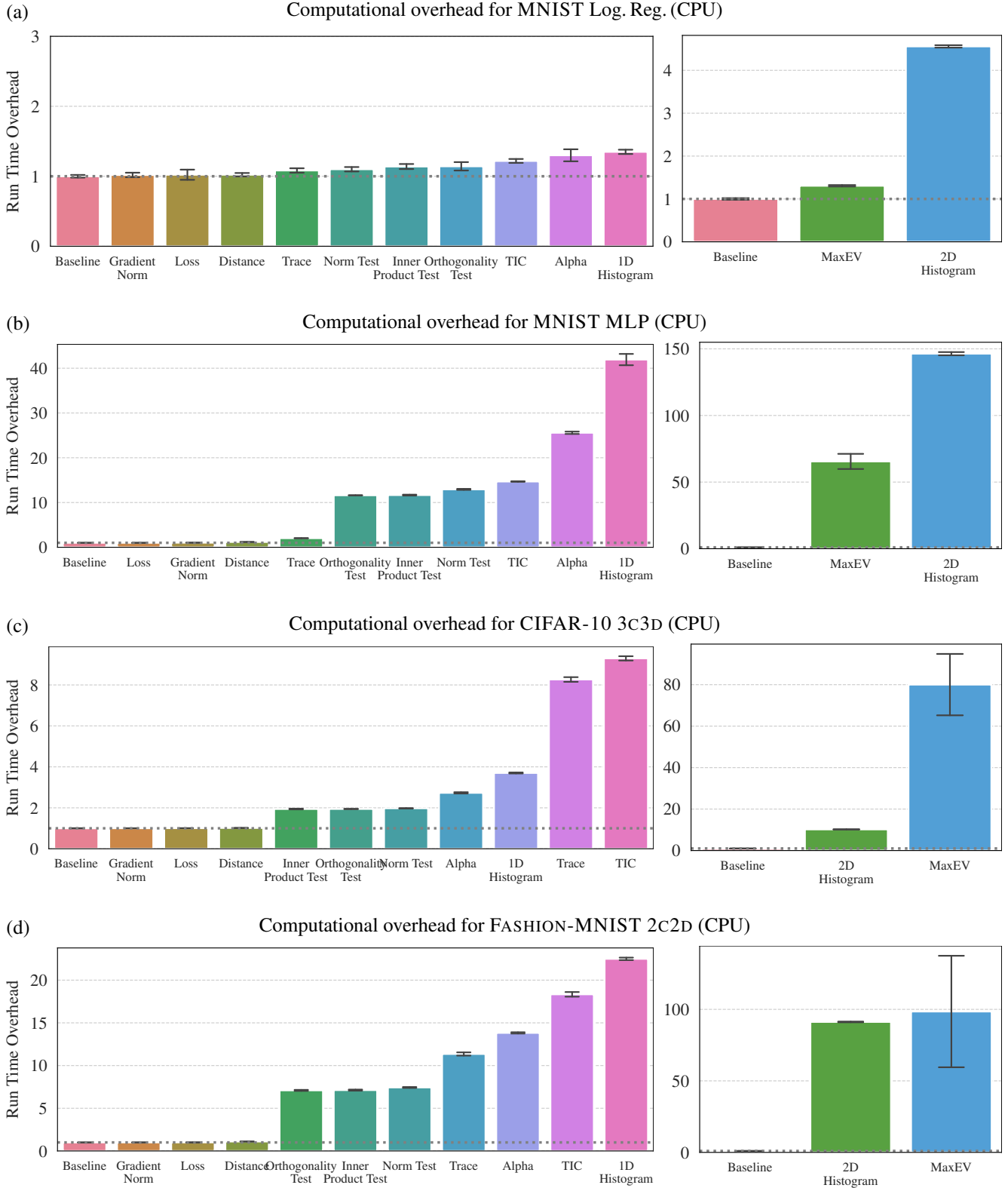


Figure 12. **Individual overhead of COCKPIT’s instruments on CPU for four different problems.** All run times are shown as multiples of the *baseline* without tracking. Expensive quantities are displayed in separate panels on the right. Experimental details in the text.

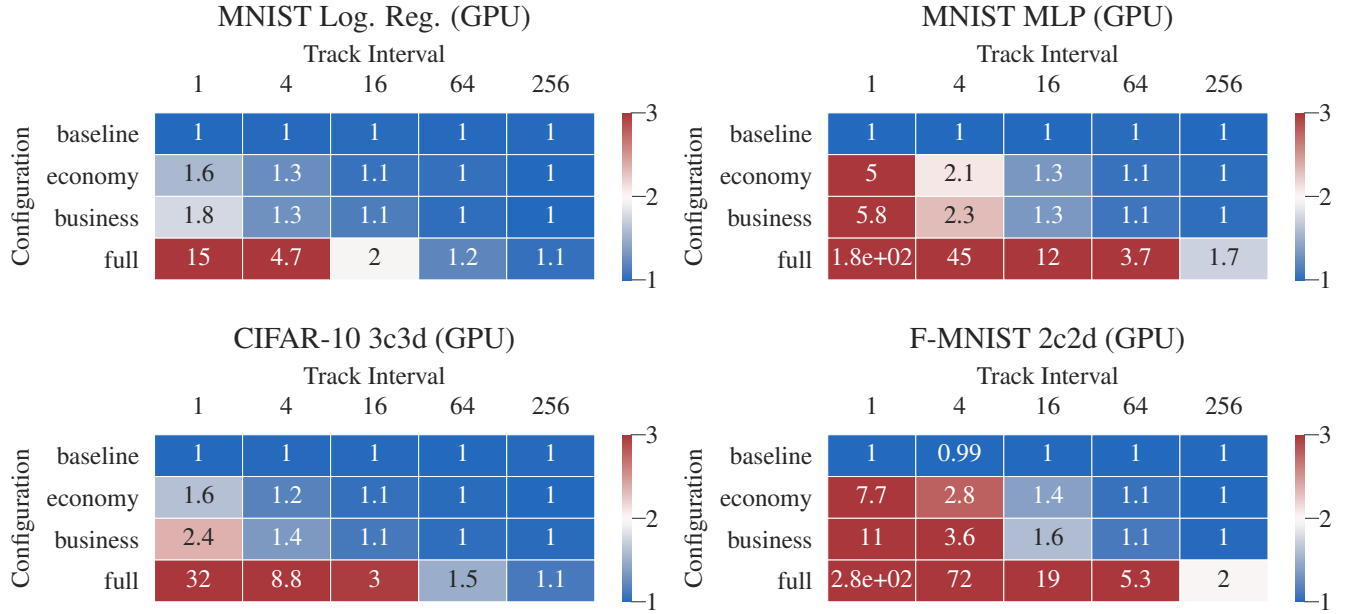


Figure 13. Overhead of COCKPIT configurations on GPU for four different problems with varying tracking interval.

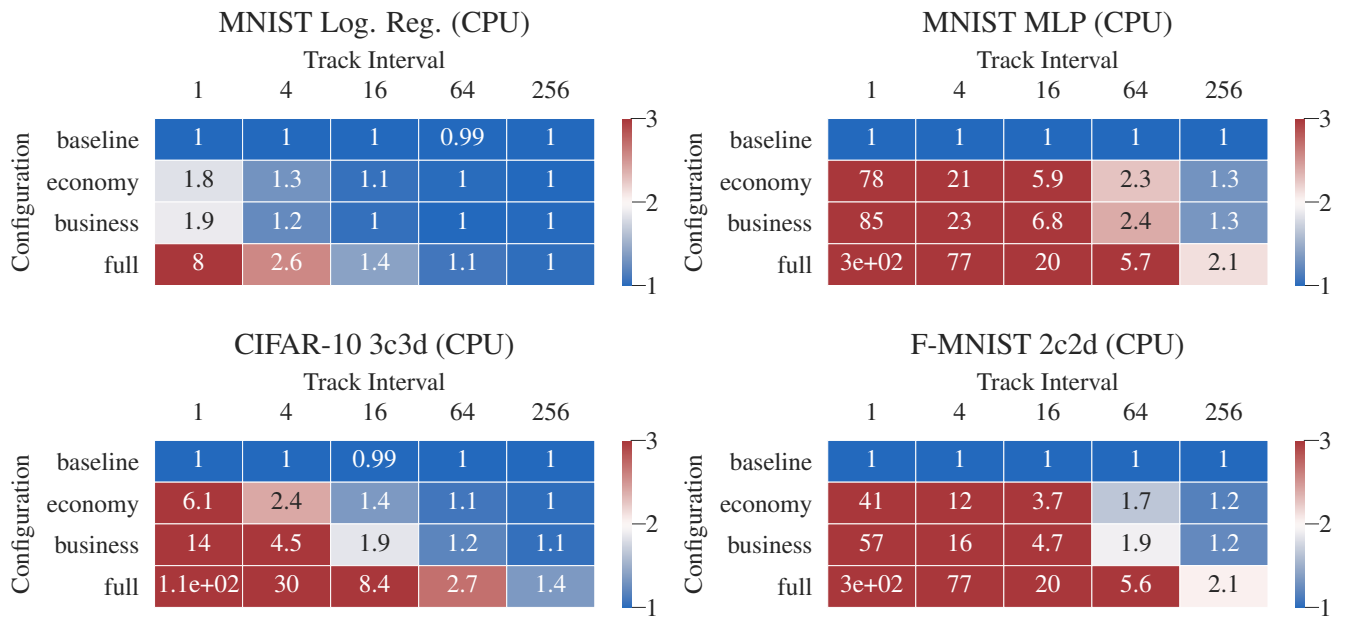


Figure 14. Overhead of COCKPIT configurations on CPU for four different problems with varying tracking interval.

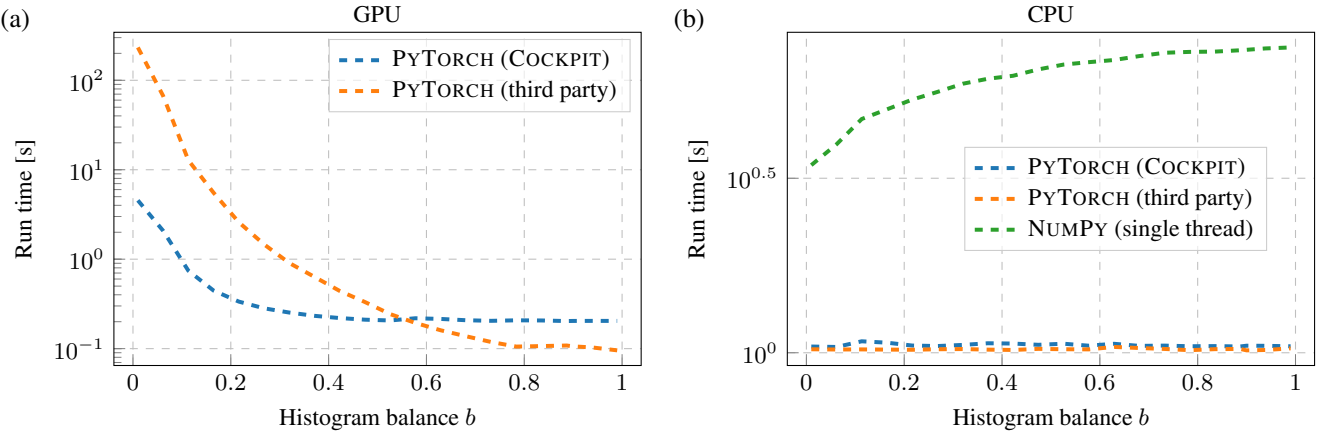


Figure 15. **Performance of two-dimensional histogram GPU implementations depends on the data.** (a) Run time for two different GPU implementations with histograms of different imbalance. COCKPIT’s implementation outperforms the third party solution by more than one order of magnitude in the deep learning regime ($b \ll 1$). (b) On CPU, performance is robust to histogram balance. The run time difference between NUMPY and PYTORCH is due to multi-threading. Data has the same size as DEEPOBS’s CIFAR-10 3C3D problem ($D = 895, 210, |\mathcal{B}| = 128$). Curves represent averages over 10 independent runs. Error bars are omitted to improve legibility.

C.3. Performance of two-dimensional histograms:

Both one- and two-dimensional histograms require $|\mathcal{B}| \times D$ elements be accessed, and hence perform similarly. However, we observed different behavior on GPU and decided to omit the two-dimensional histogram’s run time in the main text. As explained here, this performance lack is not fundamental, but a shortcoming of the GPU implementation. PYTORCH provides built-in functionality for computing one-dimensional histograms at the time of writing, but is not yet featuring multi-dimensional histograms. We experimented with three implementations:

- **PYTORCH (third party):** A third party implementation⁴ under review for being integrated into PYTORCH⁵. It relies on `torch.bincount`, which uses `atomicAdd`s that represent a bottleneck for histograms where most counts are contained in one bin⁶. This occurs often for over-parameterized deep models, as most of the gradient elements are zero.
- **PYTORCH (COCKPIT):** Our implementation uses a suggested workaround, computes bin indices and scatters the counts into their associated bins with `torch.Tensor.put_`. This circumvents `atomicAdd`s, but has poor memory locality.
- **NUMPY:** The single-threaded `numpy.histogram2d` serves as baseline, but does not run on GPUs.

To demonstrate the strong performance dependence on the data, we generate data from a uniform distribution over $[0, b] \times [0, b]$, where $b \in (0, 1)$ parametrizes the histogram’s balance, and compute two-dimensional histograms on $[0, 1] \times [0, 1]$. Figure 15 (a) shows a clear increase in run time of both GPU implementations for more imbalanced histograms. Note that even though our implementation outperforms the third party by more than one order of magnitude in the deep neural network regime ($b \ll 1$), it is still considerably slower than a one-dimensional histogram (see Figure 11 (c)), and even slower on GPU than on CPU (Figure 15 (b)). As expected, the CPU implementations do not significantly depend on the data (Figure 15 (b)). The performance difference between PYTORCH and NUMPY is likely due to multi-threading versus single-threading.

Although a carefully engineered histogram GPU implementation is currently not available, we think it will reduce the computational overhead to that of a one-dimensional histogram in future releases.

⁴Permission granted by the authors of https://github.com/miranov25/RootInteractive/.../histogramdd_pytorch.py

⁵See <https://github.com/pytorch/pytorch/pull/44485>.

⁶See <https://discuss.pytorch.org/t/torch-bincount-1000x-slower-on-cuda/42654>

D. COCKPIT view of convex stochastic problems

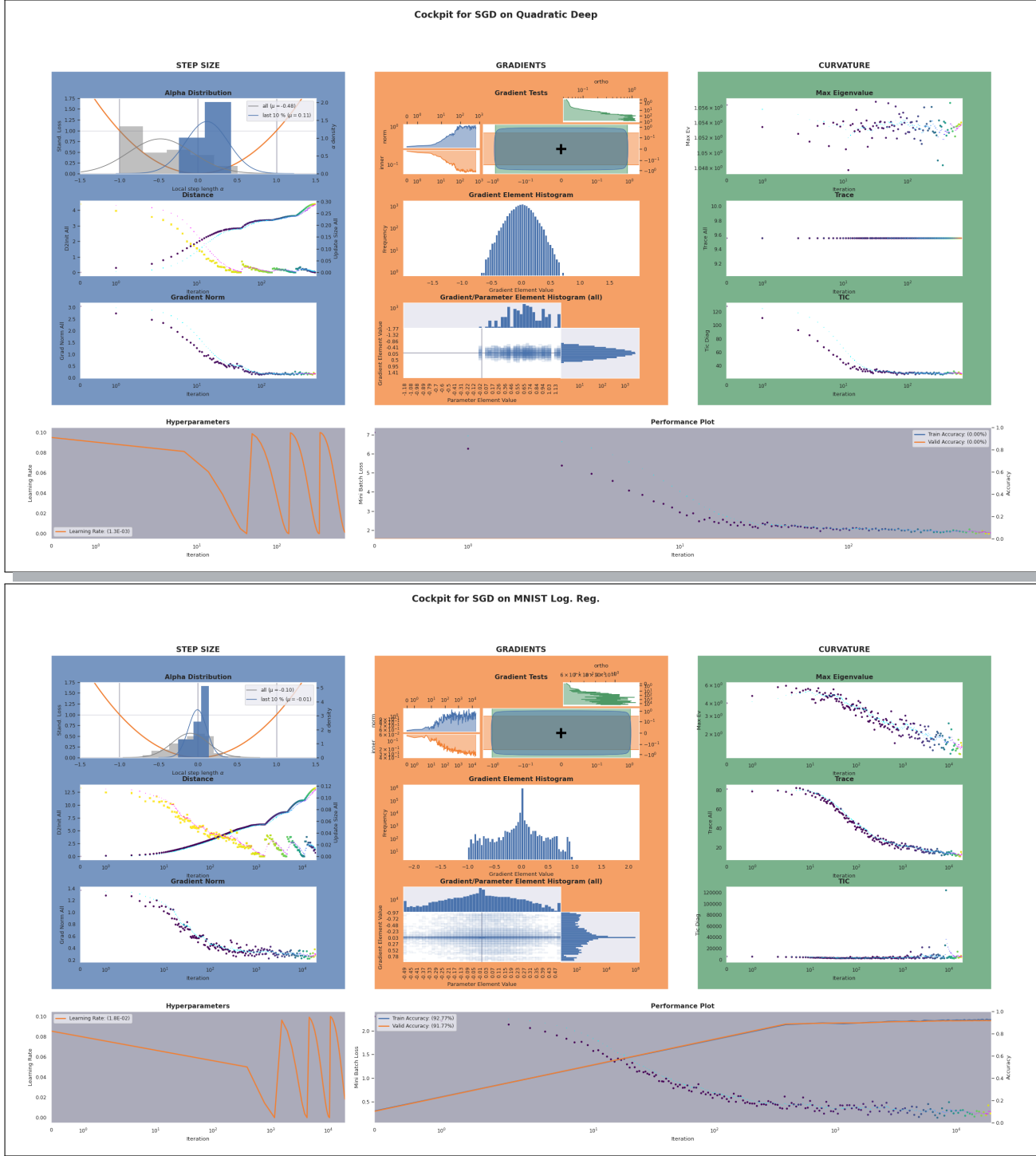


Figure 16. Screenshot of COCKPIT’s full view for convex DEEPOBS problems. Top COCKPIT shows training on a noisy quadratic loss function. Bottom shows training on logistic regression on MNIST. Figure and labels are not meant to be legible. It is evident, that there is a fundamental difference in the optimization process, compared to training deep networks, *i.e.* Figure 2. This is, for example, visible when comparing the gradient norms, which converge to zero for convex problems but not for deep learning.